Reaching Criterion of a Three-Phase Voltage-Source Inverter Operating With Passive and Nonlinear Loads and Its Impact on Global Stability

Kaustuva Acharya, *Student Member, IEEE,* Sudip K. Mazumder, *Senior Member, IEEE,* and Ishita Basu, *Student Member, IEEE*

***Abstract*—We develop and demonstrate a technique based on composite Lyapunov functions (CLFs) to analyze the impacts of passive (*RL* and *RC*) and nonlinear (diode rectifier) loads on the *reaching dynamics* of a three-phase voltage-source inverter (VSI). The *reaching criterion* (which ensures convergences of state trajectories to an orbit) is synthesized using piecewise linear models of the VSI and the loads and conditions for switching among the various models (corresponding to the different switching states). Once orbital existence is ensured using the *reaching criterion*, we extend the CLF-based approach to predict the stability of the nominal (period-1) orbit of the system (comprising the three-phase VSI and the load) and compare these predictions with those obtained using a conventional impedance-criterion technique that is developed based on a linearized averaged model. Overall, we demonstrate the significance of analyzing the reaching condition from the standpoint of orbital existence and why such a criterion is necessary for analyzing global stability. On a broader note, the methodology outlined in this paper is useful for analyzing the global stability of multiphase inverters, potentially leading to advanced control design of VSI for applications including uninterrupted power supplies, telecommunication power supplies, grid-connected inverters, motor drives, and active filters.**

***Index Terms*—Converter–load interactions, impedance criterion, linear matrix inequality (LMI), Lyapunov's stability, piecewise linear (PWL) systems, reaching conditions, three-phase inverters.**

I. Introduction

INTERACTIONS among power converters, input/output filters, and their loads have been investigated in great detail over the years for dc/dc converters [1]–[6] and, recently, for multivariable systems including three-phase inverters and rectifiers in the synchronous reference frame [7]. These techniques predict the regions of stable operation with varying loads and input conditions and are used to determine control strategies and controller bandwidths/gains to ensure operation within stability bounds. However, these techniques are based on the linear systems theory, and their predictions may be inadequate for certain operating conditions of switching power converters, as demonstrated, for instance, in [8] for dc/dc converters. Moreover, these techniques cannot account for cases where nonlinear loads (e.g., diode rectifier loads) are connected to the converter. To address the issues of load nonlinearities, a technique is developed in [9] where the nonlinear load is decomposed into several linear (harmonic) loads and the impedance criterion is extended for each of the decomposed harmonics.

Although the techniques in [8] and [9] can handle nonlinearities due to switching and nonlinear loads, respectively, they (as well as the methodologies outlined in [1]–[7]) assume orbital existence. Therefore, these techniques cannot be used to predict the global stability of converters. For global stability predictions, the reaching criterion for orbital existence has to be established first. Traditionally, the reaching dynamics of the system are investigated using time-domain simulations of the system model [10]–[12]. Over the years, significant research effort has been devoted to developing techniques for faster simulations; for instance, by using s-domain techniques to solve the differential equation that governs the system dynamics in each switching state [13] or by tracking the envelope of the state trajectories during large-signal perturbations [14]. However, these simulation-based approaches sacrifice the accuracy of the system models (as in [14]) either by ignoring the switching discontinuities or because of the limitations of the simulation algorithm (sampling time and truncation errors as in [13]). Furthermore, depending on how long the model has to be simulated and due to the possibility of a large number of initial conditions, simulation-based techniques for large-signal stability analyses can have a significant computational overhead, particularly as the dimension and number of switching states of the model increase.

Therefore, there exists a need to develop analytical techniques to analyze the large-signal stability of power converters. Some such analytical approaches have been developed in [15]–[18]. However, all of these techniques are either computationally cumbersome [15] for large-dimension systems or are limited to certain specific convergence mechanisms [16]–[18]. The limitations of some of the existing analytical techniques for reaching condition analyses have been summarized in detail in [19], where the authors describe a technique based on composite Lyapunov functions (CLFs) to determine the reaching condition for orbital existence of switching power converters. In conjunction with existing linear and nonlinear techniques

Manuscript received March 30, 2007; revised December 18, 2007. This work was supported by the National Science Foundation (NSF) under CAREER Award 0239131 and in part by the Office of Naval Research (ONR) under Young Investigator Award N000140510594.

The authors are with the Laboratory for Energy and Switching-Electronics Systems, Department of Electrical and Computer Engineering, University of Illinois, Chicago, IL 60607 USA (e-mail: mazumder@ece.uic.edu).

Color versions of one or more of the figures in this paper are available online at http://ieeexplore.ieee.org.

Digital Object Identifier 10.1109/TIE.2008.917101

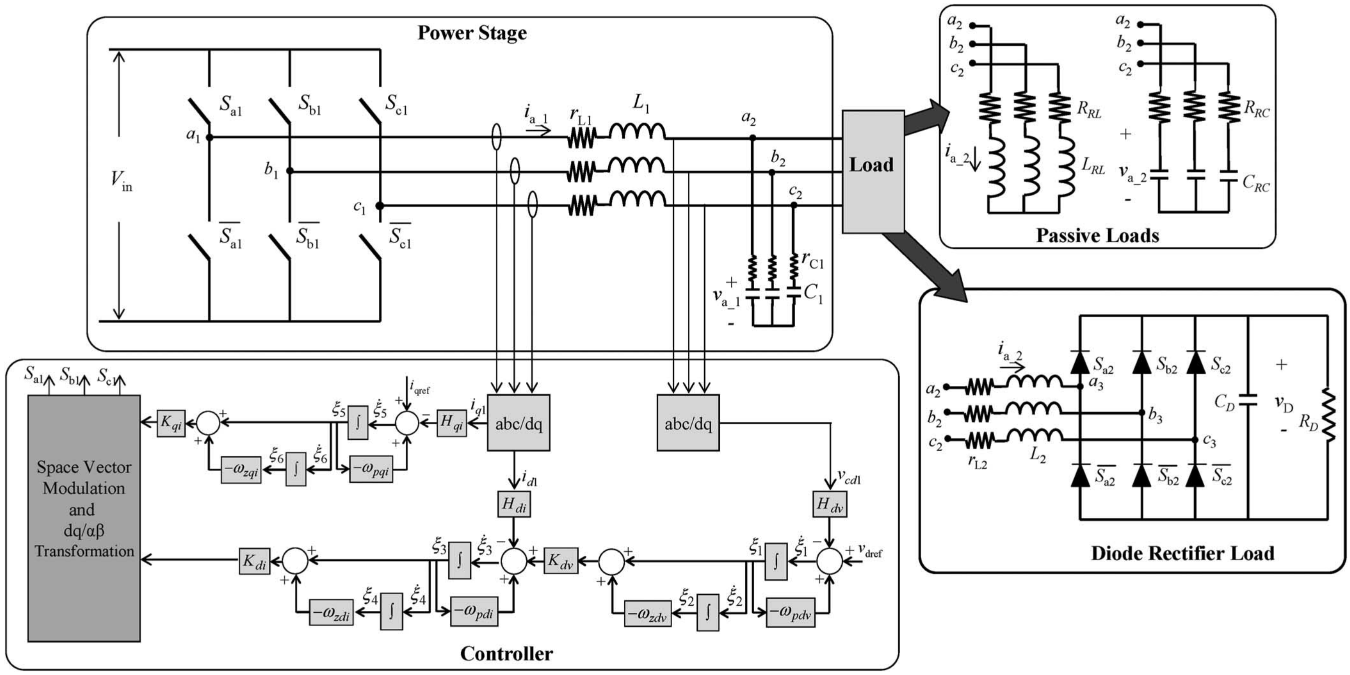

Fig. 1. Schematic of the overall VSI-load system, comprising the power stage and feedback controller connected to two passive load types and a three-phase diode rectifier load. The conventional symmetrical space-vector modulation scheme is used [24]. For the passive loads, the parasitic resistances of the inductor L_{RL} and the capacitor C_{RC} are assumed to be lumped with the series resistors (R_{RL} and C_{RC}, respectively).

for steady-state stability, the reaching criterion in [19] can be applied to analytically determine the global stability of certain classes of switching power converters [20].

In this paper, we investigate the impacts of different load types (constant and pulsating passive *RL* and *RC* loads, and a nonlinear diode rectifier load) on the reaching conditions of a three-phase voltage-source inverter (VSI) by modifying the techniques developed in [19]. Section II describes the piecewise linear (PWL) models of the three-phase VSI with different load types. In Section III, we develop the reaching criterion for the VSI-load system using a CLF-based approach. In Section IV, we describe how this technique can be extended to predict the stability of the nominal (period-1) orbit of the VSI-load system. Finally, in Section V, we present the results of the analyses and determine the reachability bounds of the VSI-load system. Furthermore, we demonstrate how the lack of knowledge of reachability can yield inaccurate global stability results. From the point of view of multiphase inverter design, global-stability predictions using the CLF-based methodology is a powerful tool for robust stability analysis and control design for a wide range of applications including uninterrupted power supplies, telecommunication power supplies, grid-connected inverters, motor drives, and active filters [21]–[23].

II. PWL Models of VSI With Passive and Diode Rectifier Loads

In this section, we derive PWL state-space models of the three-phase VSI and the different loads and define the conditions that govern switching among these PWL models. The reaching criterion developed in Section III and the CLF-based orbital stability analyses technique in Section IV are derived using these models. Note that, in this paper, we ignore the notation of time, i.e., we represent any state $y(t)$ as y.

A. Power-Stage Model

Fig. 1 illustrates the schematic of a three-phase VSI with two types of loads: 1) linear passive loads (*RC* and *RL*) and 2) a nonlinear load (three-phase diode rectifier). The voltage at points a_1, b_1, and c_1 of the VSI are given by

$$v_{a1} = \frac{2}{3}(2S_{a1} - S_{b1} - S_{c1})V_{\rm in} \tag{1a}$$

$$v_{b1} = \frac{2}{3}(-S_{a1} + 2S_{b1} - S_{c1})V_{\rm in} \tag{1b}$$

$$v_{c1} = \frac{2}{3}(-S_{a1} - S_{b1} + 2S_{c1})V_{\rm in} \tag{1c}$$

where S_{a1}, S_{b1}, and S_{c1} are the switching functions of the power devices of the three-phase VSI and are determined based on the outputs of the feedback controller, and $S_{a1} + \overline{S}_{a1} = 1$, $S_{b1} + \overline{S}_{b1} = 1$, and $S_{c1} + \overline{S}_{c1} = 1$ (neglecting dead times between the turn-on and turn-off conditions of the power devices in the same leg). The dynamics of the power stage of the three-phase VSI (shown in Fig. 1) can be described by the following vector differential equations:

$$\frac{di_1^{abc}}{dt} = K_1 i_1^{abc} + K_2 i_2^{abc} + K_3 v_1^{abc} + K_4 v_2^{abc} + K_5 V_{\rm in} \tag{2a}$$

$$\frac{dv_1^{abc}}{dt} = K_6 i_1^{abc} + K_7 i_2^{abc} + K_8 v_1^{abc} + K_9 v_2^{abc} + K_{10} V_{\rm in} \tag{2b}$$

where any vector y_r^{abc} can be represented as $y_r^{abc} = [\,y_{a\_r} \quad y_{b\_r} \quad y_{c\_r}\,]^T$. Matrices K_1–K_{10} are described in the

Appendix. We note that, in (2a), matrix K_5 contains switching functions S_{a1}, S_{b1}, and S_{c1}. The following differential equations describe the dynamics of three commonly used loads:

$$\text{Inductive Load}: \frac{di_2^{abc}}{dt} = \overline{L}_1 i_1^{abc} + \overline{L}_2 v_1^{abc} + \overline{L}_3 i_2^{abc} \tag{3a}$$

$$\text{Capacitive Load}: \frac{dv_2^{abc}}{dt} = \overline{L}_4 i_1^{abc} + \overline{L}_5 v_1^{abc} + \overline{L}_6 v_2^{abc} \tag{3b}$$

$$\text{Diode rectifier Load}: \frac{di_2^{abc}}{dt} = \overline{L}_7 v_1^{abc} + \overline{L}_8 i_2^{abc} + \overline{L}_9 v_D$$
$$\frac{dv_D}{dt} = \overline{L}_{10} i_{abc\_2} + \overline{L}_{11} v_D \tag{3c}$$

where $v_D \in \Re^{1\times 1}$ is the voltage across the output capacitor of the diode rectifier, and matrices $\overline{L}_1$–$\overline{L}_{11}$ are defined in the Appendix. For the diode rectifier load, the terms $\overline{L}_9$ and $\overline{L}_{11}$ contain the switching functions of the diodes S_{a2}, S_{b2}, and S_{c2}, due to which the model in (3c) is nonlinear. However, unlike the switching states of the VSI, which are determined based on the outputs of the feedback controller, the switching states of the diode rectifier depend on the states of the VSI and load power stages (v_1^{abc}, i_2^{abc}, and v_D) and are described in the Appendix. We note that, for the models of the VSI in (2a) and (2b), as well as for the diode rectifier model in (3c), we assume that the switches are ideal (i.e., they have no ON-state drops and have negligible rise and fall times, as well as no reverse recovery effects in case of the diodes). Combining (2a) and (2b) with (3a)–(3c), the state-space equations of the overall power stage can be expressed as

$$\frac{dx_p^{abc}}{dt} = A_{p\_j}^{abc} x_p^{abc} + B_{p\_j}^{abc} \tag{4}$$

where $x_p^{abc} = [\,(i_1^{abc})^T \quad (v_1^{abc})^T \quad (i_2^{abc})^T \quad (v_2^{abc})^T \quad v_D\,]^T$. The value of subscript j depends on the switching functions of the VSI. Using Park's transformation [24], we convert the system of equations in the stationary reference frame (4) to the synchronous reference frame. The resulting state-space equation can be expressed as

$$\frac{dx_p^{dq}}{dt} = A_{p\_i}^{dq} x_p^{dq} + B_{p\_i}^{dq} \tag{5}$$

where i represents the switching states of the synchronous reference frame model of the VSI-load system, $x_p^{dq} = T \times x_p^{abc}$ represent the states of the power stage in the synchronous reference frame, and T is the Park's transformation matrix. Matrices $A_{p\_i}^{dq}$ and $B_{p\_i}^{dq}$ are defined in the Appendix.

B. Power-Stage Model for Periodically Pulsating Loads

The state-space equation (5) describes the dynamics of the VSI when the load does not change dynamically. For time-varying loads (for instance, a periodically pulsating load, as illustrated in Fig. 2), the state-space (5) has to be modified. The dynamics of the periodically-pulsating load (d) can be represented by a Fourier series as

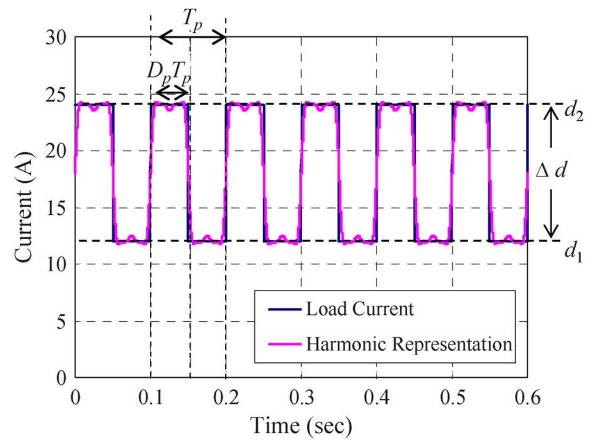

Fig. 2. Schematic illustrating a pulsating load d and its representation as a sum of harmonic components. For the latter, we ignore harmonic components $n > 11$. As illustrated, d_1 and d_2 are the two load levels, Δd is the magnitude of the load pulse perturbation ($\Delta d = d_2 - d_1$), T_p and D_p are the time period and duty ratio of the pulse, respectively.

$$d = \frac{1}{2}a_0 + \sum_{n=1}^{\infty}\{a_n \cos\omega_n t + b_n \sin\omega_n t\} \tag{6}$$

where the Fourier coefficients are given by $a_n = (1/T_p)\int_0^{T_p} d\cos(\omega_n t)dt$ and $b_n = (1/T_p)\int_0^{T_p} d\sin(\omega_n t)dt$, and $\omega_n = (2n\pi/T_p)$ represents the frequency of the nth harmonic component. The dimension of a_n and b_n is the same as that of x_p^{dq}. For the pulsating load in Fig. 2, the expressions for the Fourier coefficients are given as follows [25]:

$$a_0 = \langle d\rangle$$
$$a_n = \frac{\sin(2n\pi D_p)}{n\pi}(d_2 - d_1)$$
$$b_n = \frac{1}{n\pi}(d_2 - d_1)\{1 - \cos(2n\pi D_p)\}$$

where $\langle d\rangle$ is the average value of the load, D_p is the duty ratio of the load pulse, and d_1 and d_2 are the two levels of the pulsating load. Using the expression for d in (6), the state-space equations of the VSI with periodic loads can be expressed as

$$\frac{dx_p^{dq}}{dt} = A_{p\_i}^{dq} x_p^{dq} + B_{p\_i}^{dq} + \left(\frac{1}{2}a_0 + \sum_{n=1}^{\infty} a_n \cos\omega_n t + b_n \sin\omega_n t\right). \tag{7}$$

Next, for each frequency component in (7), we define an additional state $y_{n1} = a_n \cos\omega_n t + b_n \sin\omega_n t$. The dynamics of the states of the nth harmonic component can be described as [26]

$$y_{n1} = a_n \cos\omega_n t + b_n \sin\omega_n t$$
$$\frac{dy_{n1}}{dt} = -a_n\omega_n \sin\omega_n t + b_n\omega_n \cos\omega_n t = y_{n2}$$
$$\frac{dy_{n2}}{dt} = -a_n\omega_n^2 \cos\omega_n t - b_n\omega_n^2 \sin\omega_n t = -\omega_n^2 y_{n1}. \tag{8}$$

Using (8), the state-space (7) can be modified as

$$\frac{dx_p^{dq}}{dt} = A_{p\_i}^{dq} x_p^{dq} + B_{p\_i}^{dq} + \left(\frac{1}{2}a_0 + \sum_{n=1}^{\infty} y_{n1}\right) \tag{9}$$

with the introduction of additional state-space equations to describe the dynamics of each harmonic component. Using (8) and (9), the augmented state-space equation of the overall VSI-load system can be expressed as

$$\frac{d\hat{x}_p^{dq}}{dt} = \hat{A}_{p\_i}^{dq} \hat{x}_p^{dq} + \hat{B}_{p\_i}^{dq} \tag{10}$$

where

$$\hat{x}_p^{dq} = \begin{bmatrix} x_p^{dq} & y_{11} & y_{12} & \cdots & y_{\infty 1} & y_{\infty 2} \end{bmatrix}^T$$

$$\hat{B}_{p\_i}^{dq} = \left[\left(B_{p\_i}^{dq} + \tfrac{a_0}{2}\right) \quad 0 \quad 0 \quad \cdots \quad 0 \quad 0\right]^T$$

$$\hat{A}_{p\_i}^{dq} = \begin{bmatrix} A_{p\_i}^{dq} & 1 & 0 & \cdots & 1 & 0 \\ 0 & 0 & 1 & \cdots & 0 & 0 \\ 0 & -\omega_1^2 & 0 & \cdots & 0 & 0 \\ \vdots & \vdots & \vdots & \ddots & \vdots & \vdots \\ 0 & 0 & 0 & \cdots & 0 & 1 \\ 0 & 0 & 0 & \cdots & -\omega_\infty^2 & 0 \end{bmatrix}.$$

The dimensions of the matrices and vectors in (10) are infinite. However, for practical purposes, we use only the dominant harmonic components for our analyses to reduce computational overhead.

C. Controller Model

The closed-loop controller for the VSI-load system is implemented in the synchronous reference frame, as illustrated in Fig. 1. The d-axis controller consists of a voltage loop, which generates the reference for the current loop. The reference for the q-axis current loop is internally generated, depending on the type of load that is connected to the VSI. For all the control loops, conventional linear compensators are used. The outputs of the d-axis and q-axis current loops are modulated using a symmetrical space-vector modulation scheme [24]. Note that the analysis techniques described in this paper can be applied to other modulation schemes as well. As illustrated in Fig. 1, the compensators in the d-axis and q-axis control loops introduce additional states. The state-space equation of the controller is given by

$$\frac{dx_c}{dt} = A_c x_c + H_p x_p^{dq} + B_c \tag{11}$$

where $x_c = [\xi_1 \quad \xi_2 \quad \xi_3 \quad \xi_4 \quad \xi_5 \quad \xi_6]^T$ are the states of the controller, as shown in Fig. 1; $B_c = [v_{d\mathrm{ref}} \quad 0 \quad i_{q\mathrm{ref}} \quad 0 \quad 0 \quad 0]^T$; H_p is the matrix of the sensor gains (given in the Appendix for the different load types); and

$$A_c = \begin{bmatrix} -\omega_{pdv} & 0 & 0 & 0 & 0 & 0 \\ 1 & 0 & 0 & 0 & 0 & 0 \\ K_{dv} & K_{dv}\omega_{zdv} & -\omega_{pdi} & 0 & 0 & 0 \\ 0 & 0 & 1 & 0 & 0 & 0 \\ 0 & 0 & 0 & 0 & -\omega_{pqi} & 0 \\ 0 & 0 & 0 & 0 & 1 & 0 \end{bmatrix}.$$

D. Overall Closed-Loop System Model

Combining (5) and (11) for the three loads described in Section II-A and combining (10) and (11) for the periodically pulsating load described in Section II-B, the overall state-space equation of the system is described as

$$\frac{dx}{dt} = A_i x + B_i \tag{12}$$

where $x = \begin{bmatrix} x_p^{dq} \\ x_c \end{bmatrix}$, $A_i = \begin{bmatrix} A_{p\_i}^{dq} & 0_{r\times s} \\ H_p & A_c \end{bmatrix}$, and $B_i = \begin{bmatrix} B_{p\_i}^{dq} \\ B_c \end{bmatrix}$ for the loads described in Section II-A, and $x = \begin{bmatrix} \hat{x}_p^{dq} \\ x_c \end{bmatrix}$, $A_i = \begin{bmatrix} \hat{A}_{p\_i}^{dq} & 0_{r\times s} \\ H_p & A_c \end{bmatrix}$, and $B_i = \begin{bmatrix} \hat{B}_{p\_i}^{dq} \\ B_c \end{bmatrix}$ for the pulsating load described in Section II-B. Here, all of the elements of matrix $0_{r\times s}$ are zeros.

For the VSI, the switching conditions of the power devices in the synchronous reference frame depend on the outputs of the feedback controller states and are given by

$$S_{d1} = \begin{cases} 0, & (K_{di}\xi_3 + K_{di}\omega_{zdi}\xi_4) - V_{\mathrm{mod}\,1} \le 0 \\ 1, & (K_{di}\xi_3 + K_{di}\omega_{zdi}\xi_4) - V_{\mathrm{mod}\,1} > 0 \end{cases}$$

$$S_{q1} = \begin{cases} 0, & (K_{qi}\xi_5 + K_{qi}\omega_{zqi}\xi_6) - V_{\mathrm{mod}\,1} \le 0 \\ 1, & (K_{qi}\xi_5 + K_{qi}\omega_{zqi}\xi_6) - V_{\mathrm{mod}\,1} > 0. \end{cases} \tag{13}$$

The diode rectifier load introduces additional switching states in the state-space equations of the overall system, apart from those of the original VSI. These switching states are due to the uncontrolled switching of the diodes and depend on the voltage across the diode. The switching states of the diode rectifier load can be expressed as (14), shown at the bottom of the next page. Variables $a_{35} - a_{47}$ are given in the Appendix.

III. Synthesis of Reaching Criterion

As illustrated in Fig. 3, the dynamics of the three-phase VSI consists of 1) the *reaching phase*, which describes the dynamics of the state trajectories from a given initial condition to the orbit, and 2) the *steady-state phase*, where the error trajectories of the system correspond to a periodic orbit.

To derive the reaching criterion of the VSI-load system, we first translate the state-space equation of the overall system given by (12) to the error coordinates using $e = x^* - x$, where e represents the error vector and x^* represents the steady-state

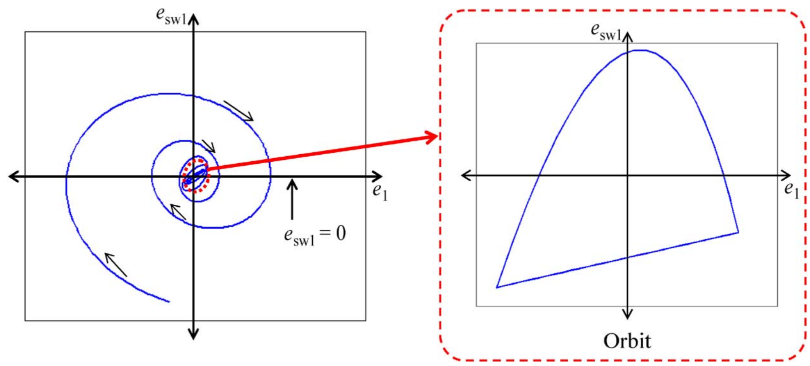

Fig. 3. Schematic illustrating the dynamics of a three-phase VSI (or any switching power converter, in general) in the *reaching* and *steady-state* (corresponding to a periodic orbit) phases of operation. Symbol $e_{sw1} = 0$ describes a switching surface, whereas e_1 represents the dynamics of one of the states of the VSI in error coordinates.

values (corresponding to infinite switching frequency) of the states. The modified state-space equation is given by

$$\frac{de}{dt} = A_i e + \overline{B}_i \tag{15}$$

where $\overline{B}_i = -(B_i + A_i x^*)$.

The reaching criterion of the VSI-load system depends on the number of nonrepetitive and nonredundant switching sequences generated by the noncomplementary switching functions of the VSI (S_{d1} and S_{q1}) and the diode rectifier load (S_{d2} and S_{q2}). The possible switching states of the VSI-load system for the passive and diode rectifier loads are listed in Table I. For the case of the passive load, $N = 4$, whereas, for the diode rectifier load, $N = 16$. The total number of nonrepetitive and nonredundant switching sequences is given by [19], [20]

$$M = \sum_{l=1}^{2^N} \left({}^{2^N}C_l\right) = \sum_{l=1}^{2^N} \left(\frac{(2^N)!}{l!(2^N - l)}\right) \tag{16}$$

where N is the total number of switching states of the overall system.

To determine the reaching criterion of the VSI-load system, we define a CLF $V_k(e) > 0$ (for the kth switching sequence, $k = 1, 2, \ldots, M$), which is a weighted sum of the Lyapunov functions ($e^T P_{ki} e$) in each switching state of a given sequence k and is given by [27]

$$V_k(e) = \sum_{i=1}^{h} \alpha_{ki} e^T P_{ki} e, \quad k = 1, 2, \ldots, M \tag{17}$$

where h is the number of switching states in a given switching sequence k, α_{ki} are the weights of the Lyapunov functions in each switching state such that $0 \le \alpha_{ki} \le 1$ and $\sum_{i=1}^{h} \alpha_{ki} = 1$,

TABLE I
SWITCHING STATES OF THE VSI-LOAD SYSTEM

VSI and Passive Load		
i	S_{d1}	S_{q1}
1	0	0
2	0	1
3	1	0
4	1	1

VSI and Diode-rectifier Load				
i	S_{d1}	S_{q1}	S_{d2}	S_{q2}
1	0	0	0	0
2	0	0	0	1
3	0	0	1	0
4	0	0	1	1
5	0	1	0	0
6	0	1	0	1
7	0	1	1	0
8	0	1	1	1
9	1	0	0	0
10	1	0	0	1
11	1	0	1	0
12	1	0	1	1
13	1	1	0	0
14	1	1	0	1
15	1	1	1	0
16	1	1	1	1

and $P_{ki} = P_{ki}^T$ is a positive-definite matrix. Now, taking the derivative of $V_k(e)$ in (17) and using (15), we obtain the following:

$$\begin{aligned}\frac{dV_k(e)}{dt} &= \sum_{i=1}^{h} \alpha_{ki} \left(\frac{de^T}{dt} P_{ki} e + e^T P_{ki} \frac{de}{dt}\right)\\ &= \sum_{i=1}^{h} \alpha_{ki} \left(\begin{bmatrix} e \\ 1 \end{bmatrix}^T \begin{bmatrix} A_i^T P_{ki} + P_{ki} A_i & P_{ki}\overline{B}_i \\ \overline{B}_i^T P_{ki} & 0 \end{bmatrix} \begin{bmatrix} e \\ 1 \end{bmatrix}\right).\end{aligned} \tag{18}$$

$$S_{d2} = \begin{cases} 0, & \{(1 + a_{35}L_2)v_{d1} - (r_{L2} + a_{31}L_2)i_{d1} + (L_2 a_{37} - 1)v_D - L_2(a_{32}i_{q1} + a_{33}i_{d2} + a_{34}i_{q2} + a_{36}v_{q1})\} \le 0 \\ 1, & \{(1 + a_{35}L_2)v_{d1} - (r_{L2} + a_{31}L_2)i_{d1} + (L_2 a_{37} - 1)v_D - L_2(a_{32}i_{q1} + a_{33}i_{d2} + a_{34}i_{q2} + a_{36}v_{q1})\} > 0 \end{cases}$$

$$S_{q2} = \begin{cases} 0, & \{(1 + a_{46}L_2)v_{q1} - (r_{L2} + a_{42}L_2)i_{q1} + (L_2 a_{47} - 1)v_D - L_2(a_{41}i_{d1} + a_{43}i_{d2} + a_{44}i_{q2} + a_{45}v_{d1})\} \le 0 \\ 1, & \{(1 + a_{46}L_2)v_{q1} - (r_{L2} + a_{42}L_2)i_{q1} + (L_2 a_{47} - 1)v_D - L_2(a_{41}i_{d1} + a_{43}i_{d2} + a_{44}i_{q2} + a_{45}v_{d1})\} > 0 \end{cases} \tag{14}$$

As per Lyapunov's method, the error trajectories of the system converge toward the orbit for finite switching frequency (or the equilibrium point for infinite switching frequency), provided that $(dV_k(e)/dt) < 0$. This condition is satisfied by (18), provided that the following matrix inequality is satisfied:

$$\sum_{i=1}^{h} \alpha_{ki} \begin{bmatrix} A_i^T P_{ki} + P_{ki} A_i & P_{ki} \overline{B}_i \\ \overline{B}_i^T P_{ki} & 0 \end{bmatrix} < 0. \tag{19}$$

If there are no solutions of P_{ki} for (19), we investigate the dual of $V_k(e)$ to confirm that the error trajectories of the VSI do not converge to the orbit [28], [29]. We define the dual of $V_k(e)$ as

$$V_{Dk}(e) = \sum_{i=1}^{h} \lambda_{ki} e^T Q_{ki} e, \quad k = 1, 2, \ldots, M \tag{20}$$

where $0 \le \lambda_{ki} \le 1$, $\sum_{i=1}^{h} \lambda_{ki} = 1$, and $Q_{ki} = Q_{ki}^T$ is a positive-definite matrix. For the kth switching sequence, the error trajectories of the VSI do not converge to the orbit, provided that $V_{Dk}(e)$ satisfies the following criteria:

$$V_{Dk}(e) > 0 \quad \text{and} \quad \frac{dV_{Dk}(e)}{dt} > 0 \tag{21a}$$

or

$$-V_{Dk}(e) = \sum_{i=1}^{h} \lambda_{ki} e^T (-Q_{ki}) e < 0 \quad \text{and} \quad -\frac{dV_{Dk}(e)}{dt} < 0. \tag{21b}$$

Following (18) and (19), (21b) is satisfied, provided that

$$\sum_{i=1}^{h} \lambda_{ki} \begin{bmatrix} -A_i^T Q_{ki} - Q_{ki} A_i & -Q_{ki} \overline{B}_i \\ -\overline{B}_i^T Q_{ki} & 0 \end{bmatrix} < 0. \tag{22}$$

If there are no solutions of P_{ki} for (19) but there exist solutions of Q_{ki} for (22), we conclude that the system does not satisfy the reaching criterion for orbital existence.

IV. Steady-State Stability Criteria

The reaching criterion (19) derived in Section III predicts orbital existence. Once this criterion is satisfied, the next goal is to analyze the stability of the nominal (period-1) orbit of the VSI-load system. Because the dynamics of this system is fundamentally governed by a line-frequency (slow) and a switching-frequency (fast) [8] component, the frequency of the nominal (period-1) orbit is determined by the least common multiple of the two frequency components [30], [31].

Stability of the nominal orbit can be investigated using the CLF-based approach (which is explained here) by investigating the change of (17) over one nominal time period. The nominal orbit is stable, provided that $dV_k(e)/dt = 0$. Such an approach can account for both the fast-scale and slow-scale dynamics of the system [8]. Because the two frequency components in our case (and as shown in Table II) are several orders apart, for practical purposes, we assume that the frequency of the nominal orbit is the same as the slow-frequency component and subsequently investigate the change in CLF (17) over this period. By equating the left-hand side of (19) to zero, the condition for the stability of the nominal orbit can be expressed as

TABLE II
PARAMETERS OF THE THREE-PHASE VSI USED FOR SIMULATIONS

POWER STAGE		CONTROLLER	
Parameter	**Nominal Values**	**Parameter**	**Nominal Values**
Input voltage, V_{in}	400 V	d-axis voltage loop gain, K_{dv}	50
Output line-line voltage	208 Vrms	d-axis voltage loop zero, ω_{zdv}	10 rad/s
Output line frequency	60 Hz	d-axis voltage loop pole, ω_{pdv}	25000 rad/s
Power	2.5 kVA	d-axis current controller gain, K_{di}	15000
Switching frequency, f_{sw}	20 kHz	d-axis current controller zero, ω_{zdi}	1000 rad/s
VSI line inductors, L_1	1.5 mH	d-axis current controller pole, ω_{pdi}	25000 rad/s
Output filter capacitors, C_1	10 µF	q-axis current controller gain, K_{qi}	10000
Diode rectifier line inductors, L_2	5 mH	q-axis current controller zero, ω_{zqi}	100 rad/s
Diode rectifier output capacitor, C_D	1000 µF	q-axis current controller pole, ω_{pqi}	20000 rad/s

$$\sum_{i=1}^{h} \alpha_{ki} \begin{bmatrix} A_i^T P_{ki} + P_{ki} A_i & P_{ki} \overline{B}_i \\ \overline{B}_i^T P_{ki} & 0 \end{bmatrix} = 0 \tag{23}$$

where P_{ki} are positive-definite matrices, and α_{ki} ($0 \le \alpha_{ki} \le 1$ and $\sum_{i=1}^{h} \alpha_{ki} = 1$) depends on the time spent in each switching state and can be obtained using the numerical search algorithm. The switching states of the overall system are given in Table I. If there are no positive-definite matrices P_{ki} that satisfy (23), we conclude that the nominal orbit is unstable. We note that, unlike the conventional map-based approach [8], [32], [33], which ascertain the stability of (15) using a map that is derived by sequential patching of solutions corresponding to the ith switching state and hence requires knowledge of the modulation scheme, the CLF-based approach depends only on the switching states of the nominal sequence. Even if the nominal sequence changes (e.g., due to a change in the modulation scheme), (23) is true as long as the switching states in the sequence are the same.

In contrast to the CLF-based method, the conventional technique to analyze the orbital (or steady-state) stability of (15) is based on the impedance criterion [1] that is derived using a linearized averaged model of the system. According to this criterion, the stability of the VSI-load system is guaranteed, if the input impedance of the load Z_{i_load} and the closed-loop output impedance of the VSI Z_{o_inv} satisfy the following inequality:

$$|Z_{i\_\text{load}}| > |Z_{o\_\text{inv}}|. \tag{24}$$

If (24) is violated, then, for certain cases, an extended analysis of the loop gain using the Nyquist criterion needs to be carried

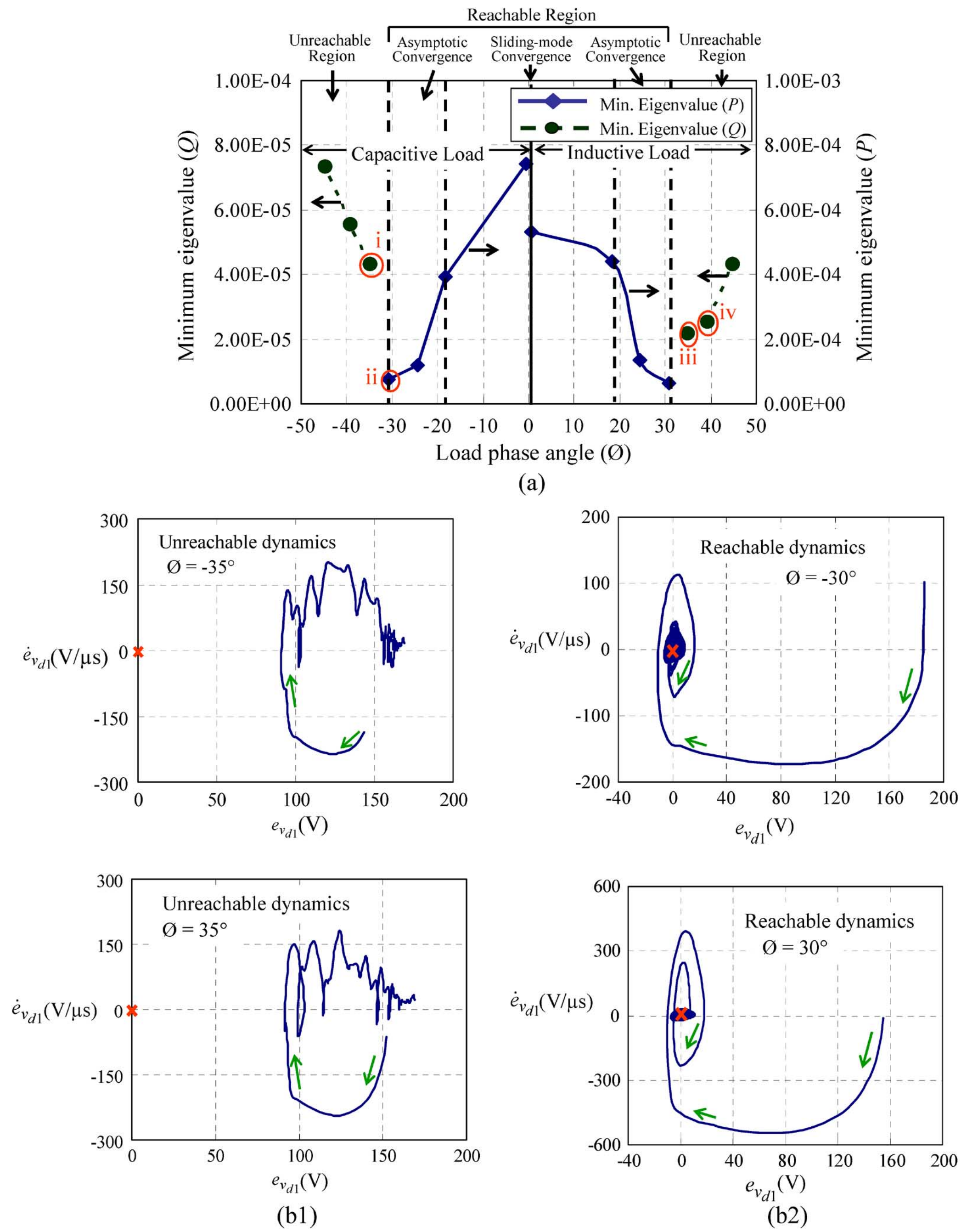

Fig. 4. (a) Plot showing the variation of the minimum eigenvalues of the augmented P and Q matrices [obtained by solving LMIs (19) and (22), respectively] with the load phase angle. The plot shows the reachable and unreachable regions of operation for the inductive and capacitive loads as well as the conditions for the sliding mode and asymptotic mode of convergence. The points marked (i)–(iv) will be used later to compare the predictions of the reaching criteria with the steady-state stability results. Simulation results illustrating the (b2) reachable and (b1) unreachable dynamics of the three-phase VSI for four operating conditions.

out to determine that the system is unstable [4], [5]. Note that this criterion is based on the averaged model and hence cannot account for the effect of fast-scale (switching-frequency) dynamics on the stability of the overall system.

V. Result

In this section, we investigate the global stability of the three-phase VSI with passive (constant and pulsating) and nonlinear loads using the reaching criterion discussed in Section III and the steady-state stability analysis techniques discussed in Section IV using the CLF-based criterion and the small-signal impedance criterion.

Matrices $P_1 \cdots P_h$ are obtained by solving linear matrix inequality (LMI) (19) (for the reachable case) and matrix equality (23) (when the nominal orbit is stable). Similarly, matrices $Q_1 \cdots Q_h$ are obtained by solving LMI (22) for the unreachable case. Because the minimum eigenvalue of a positive-definite matrix is positive, we plot the variations of the minimum eigenvalues of the augmented $P\left(=\begin{bmatrix} P_1 & 0 & 0 \\ 0 & \ddots & 0 \\ 0 & 0 & P_h \end{bmatrix}\right)$ and

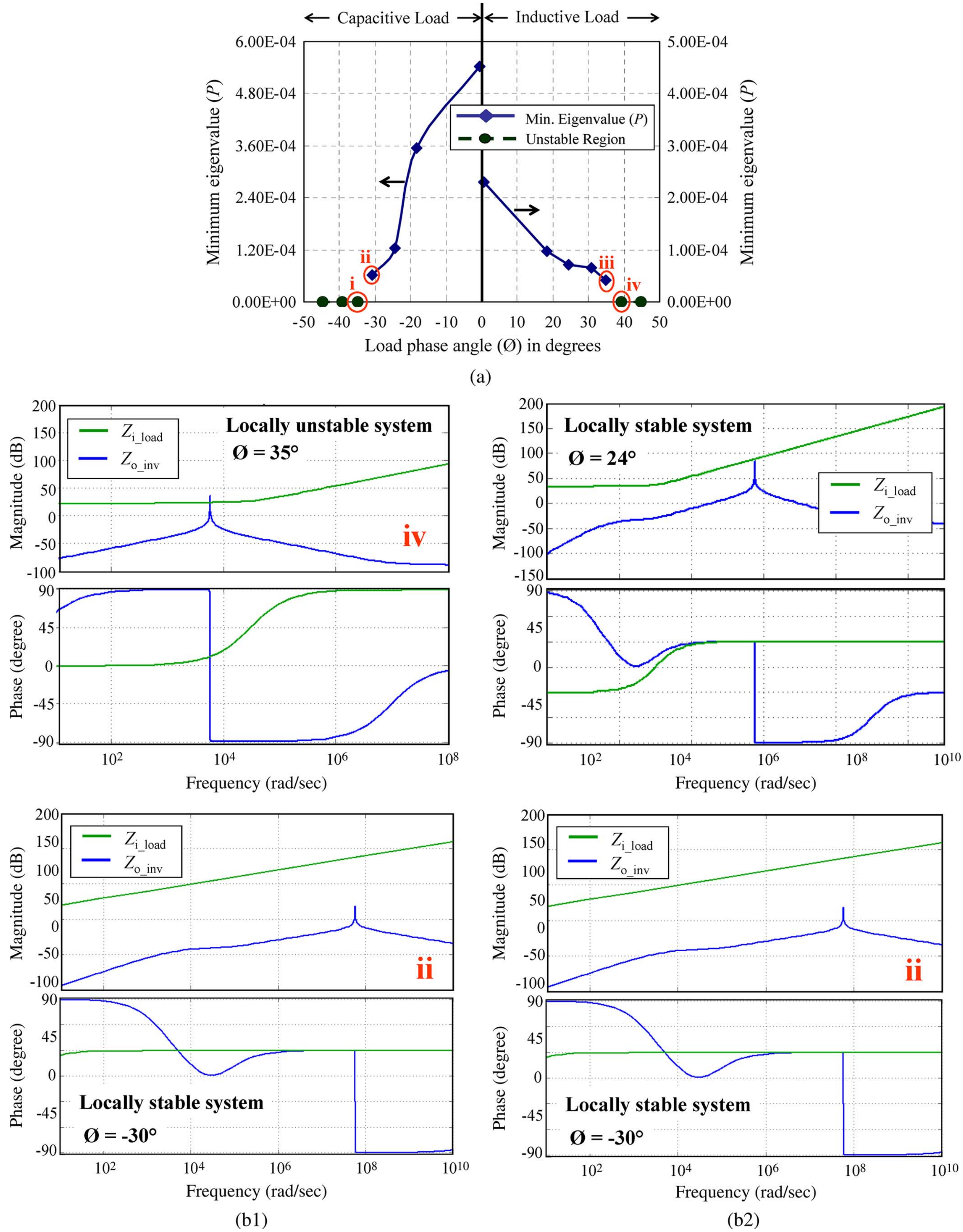

Fig. 5. (a) Plot showing the variation of the minimum eigenvalue of the augmented P matrix [obtained by solving matrix equality (23)] of a three-phase VSI with load phase angle for operating conditions where period-1 stability is satisfied. Variations of the small-signal output impedance of the VSI illustrating (b2) stable and (b1) unstable characteristics for inductive and capacitive loads, respectively, for the operating conditions identified in the figure.

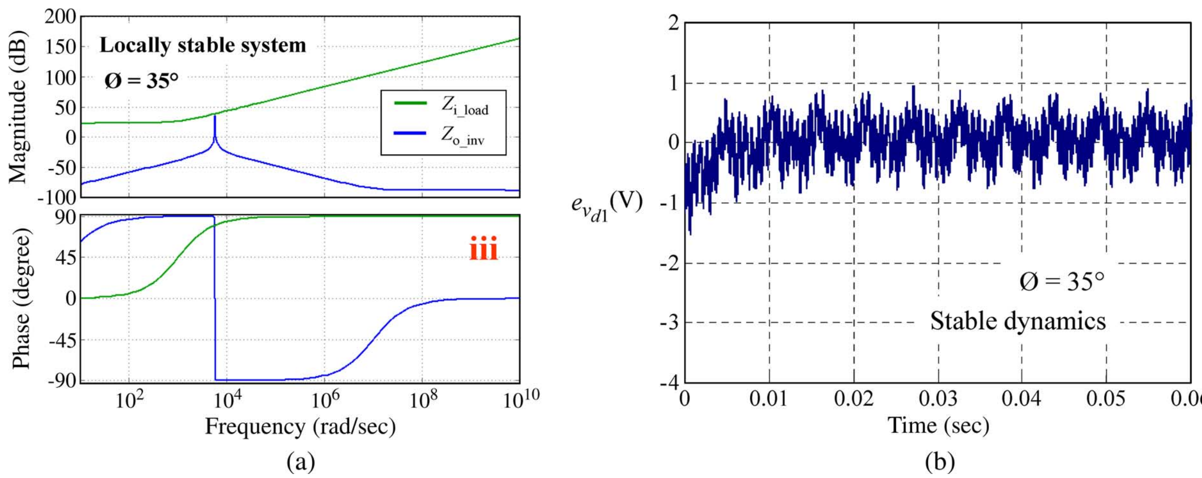

Fig. 6. (a) Variation of the small-signal output impedance of the VSI and the input impedance of the inductive load for a phase angle of $\phi = 35°$. (b) Simulation results illustrating the d-axis voltage-error of a three-phase VSI with time.

$Q\left(=\begin{bmatrix} Q_1 & 0 & 0 \\ 0 & \ddots & 0 \\ 0 & 0 & Q_h \end{bmatrix}\right)$ matrices to see if the matrices obtained by solving LMIs (19) and (22), and matrix equality (23) are positive definite. The predictions of the reaching criterion and the steady-state stability criteria are verified by time-domain simulations in *Simulink*[1]. The nominal values of the power stage and controller parameters are given in Table II.

A. *Passive Loads*

First, we investigate the impacts of the load phase angle on the *reaching conditions* of the three-phase VSI with a passive load. The variations of the minimum eigenvalues of the augmented P and Q matrices [obtained by solving LMIs (19) and (22), respectively] with the load phase angle are illustrated in Fig. 4(a). Distinction between the sliding and asymptotic modes of convergences can be obtained by using the criteria in [19] and [20]. Because sliding-mode convergence is typically faster than asymptotic convergence, this distinction can be used to design controllers with superior dynamic performance. The simulation results in Fig. 4(b1) and (b2) show the evolution of the d-axis voltage-error trajectories for the unreachable and reachable cases, respectively, for the *RC* and *RL* loads. In the simulation results, the marker (x) indicates the desired equilibrium (corresponding to zero error at infinite frequency), whereas the arrows indicate how the state-error trajectories evolve with time. For these simulations, any arbitrary initial condition is chosen. These results validate the predictions of the reaching criterion, as illustrated in Fig. 4(a).

The result in Fig. 4(a) only describes the reaching conditions for orbital existence of the VSI-load system. To comment on the global stability, we need to further analyze the stability of the nominal (period-1) orbit. Fig. 5(a) shows the variation of the minimum eigenvalues obtained by solving matrix equality (23). To obtain these results, we examine the energy balance of the system over one line cycle. However, because, in this case, the switching frequency is not an integer multiple of the line frequency, there is a small discrepancy in the energy balance over one line cycle. To avoid the large computational overhead associated with computing the energy balance over a long period of time, we consider that the nominal orbit of the system is stable if the change in $V_k(e)$ over one line cycle is bounded by a small value ε [35]. For the cases considered in this paper, these results agree with the results of the small-signal impedance criterion, given by (24), as illustrated in Fig. 5(b1) and (b2), for the inductive and capacitive loads.

Comparison of the predictions of orbital stability (Fig. 5) with those of the reaching criterion [Fig. 4(a)] indicates a discrepancy. For the inductive load, there are three parameter-dependent regions, i.e., the reachable and stable $(\phi < 30°)$, unreachable but stable $(\phi = 35°)$, and unreachable and unstable $(\phi > 35°)$ regions. For the operating condition corresponding to $\phi = 35°$ [marked (iii) in Figs. 4(a) and 5(a)], the steady-state analysis techniques predict that the system is stable, as illustrated in Figs. 5(a) and 6(a). However, the reaching criterion is not satisfied for this case. Using time-domain simulations, Fig. 6(b) illustrates that the error trajectories reach the orbit, provided that the initial condition lies within its vicinity. However, for any other arbitrary initial condition, which is not near the orbit, the error trajectories do not converge, as illustrated in Fig. 4(b1) for the corresponding case. These results demonstrate the need for reaching condition analyses, in addition to the steady-state orbital stability to predict the global stability of the VSI-load system.

Next, we investigate the impacts of load variations on the reaching conditions of the overall system for two different values of the d-axis voltage-loop compensator gain K_{dv}. Fig. 7 illustrates that the region of reachable operation shrinks with decrease in the load power. In addition, the region of reachable operation further reduces as K_{dv} is increased. By investigating the effects of other controller parameters on the reaching conditions, one can determine appropriate controller parameters for the VSI-load system for different applications. Finally, we investigate whether the rate of change of the load has any impact on the reaching conditions of the system. Here, we note

[1]The simulation models of the three-phase inverter have been verified by experimental results, which have been presented in our previous papers [19], [20].

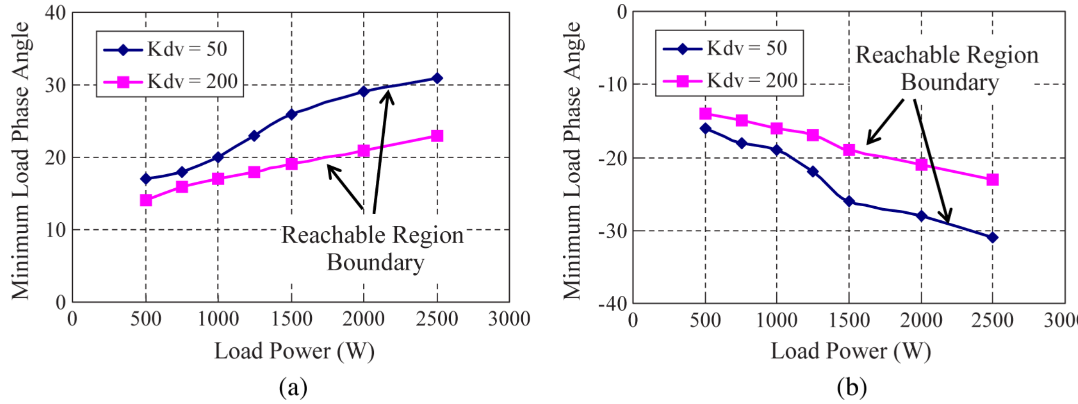

Fig. 7. Variation of the reaching conditions of the VSI-load system with changes in the load power and the d-axis voltage-loop compensator gain for (a) *RL* and (b) *RC* loads.

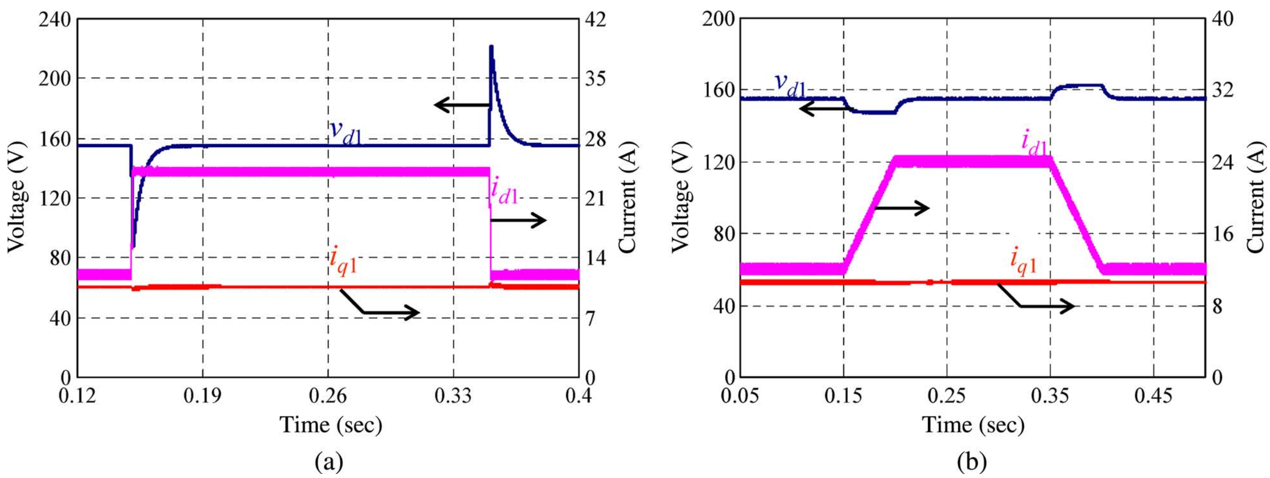

Fig. 8. Simulation results illustrating the dynamics of the three-phase VSI for a 50%–100% (of the full load) load transient for two different slew rates: (a) 12 000 and (b) 240 A/s.

that both load levels satisfy the reaching criterion for orbital existence. Fig. 8 illustrates two cases: The rates of change of the load are 1) 12 000 A/s and 2) 240 A/s. For both cases, the initial and final load conditions satisfy LMI (19), i.e., the dynamics are reachable. From Fig. 8, we observe that the reaching condition does not change with step variation of the rate of change of load. This result is true as long as the rate of change of the load is sufficiently slower than the switching frequency of the VSI-load system.

B. Pulsating Load

In the previous section, we investigated the impacts of load variations on the reaching conditions of a VSI with passive loads. In this section, we investigate the impacts of a pulsating *RL* load[2] (as shown in Fig. 2) on the reaching conditions of such a system. The pulsating load is represented by a sum of harmonic components, as described in Section II-B. For the case considered in this paper, we observe that the pulsating load is adequately described by harmonic components from $n = 1$ to $n = 11$. Therefore, to avoid a higher computation overhead, we ignore the higher order harmonic components. Fig. 9 illustrates the variation of the maximum allowable duty ratio, which corresponds to the reachable-region boundary, with variations of the magnitude and frequency of the pulsating load. The region below this surface corresponds to the reachable region. From the figure, we observe that the reachable region

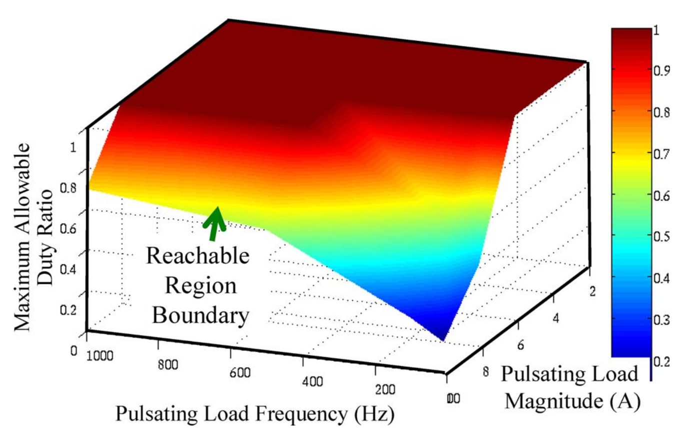

Fig. 9. Variation of the maximum allowable duty ratio (corresponding to the reachable-region boundary) with variations of the load perturbation magnitude and frequency. The duty ratio of the pulsating load is defined as the ratio of the time spent at load level d_1 with respect to load level d_2.

[2]We note that similar analyses can be performed for pulsating *RC* and diode rectifier loads as well.

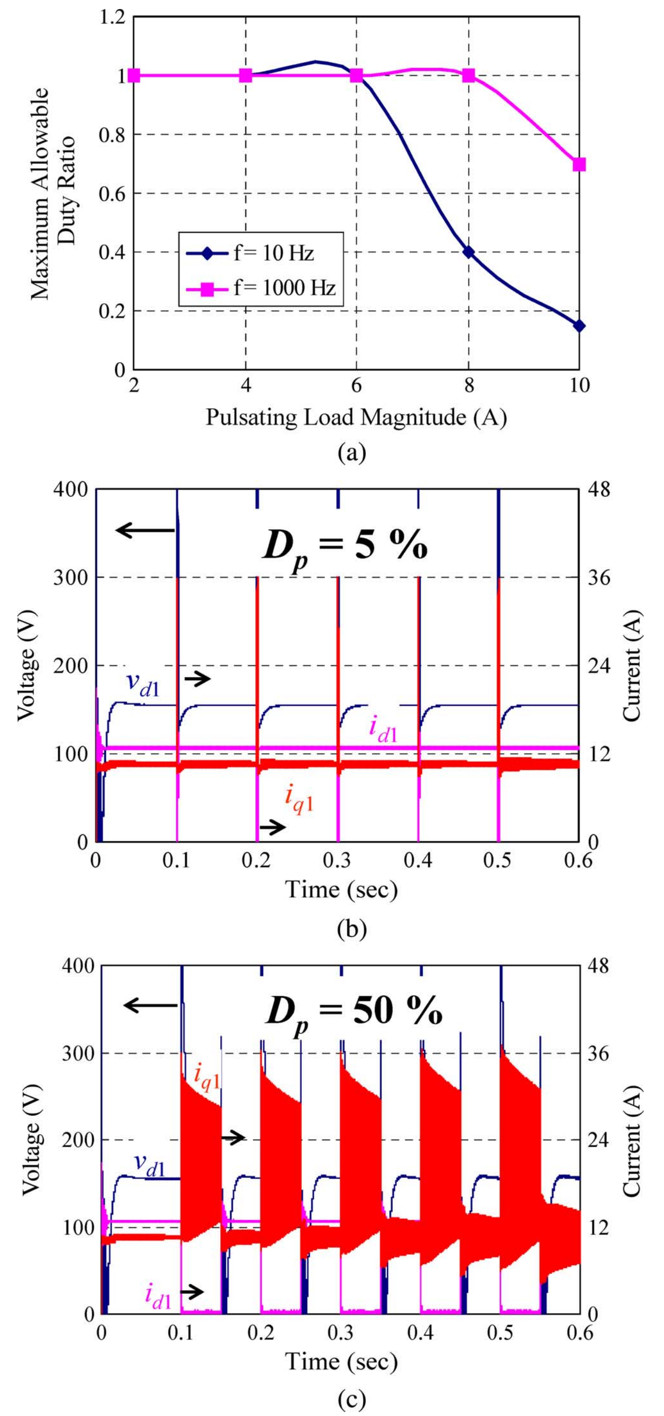

Fig. 10. (a) Variations of the maximum allowable duty ratio with perturbation magnitude for $f_p = 10$ Hz and $f_p = 1000$ Hz. (b) and (c) Simulation results illustrating the dynamics of the three-phase VSI with a pulsating load for (b) duty ratio $= 5\%$ and (c) duty ratio $= 50\%$. For the simulation results in (b) and (c), $\Delta d = 12$ A, and $f_p = 10$ Hz.

can vary with the magnitude and frequency of the load pulse. In other words, the reachable region significantly depends on the amount of time spent at each load level of the pulsating load.

Fig. 10(a) illustrates the variation of the reachable-region boundary with the magnitude of the pulsating load for two operating frequencies ($f_p = 10$ Hz and $f_p = 1000$ Hz). Here, one of the load levels d_1 satisfies the reaching conditions (from the results in Section V-A), whereas the other load level d_2 does not satisfy the reaching condition. We observe that, for low duty ratios, the system satisfies the reaching condition for orbital existence. In other words, if the time spent at load level d_2 is small, the state-error trajectories reach the orbit from an arbitrary initial condition. The simulation results in Fig. 10(b) and (c) validate these predictions.

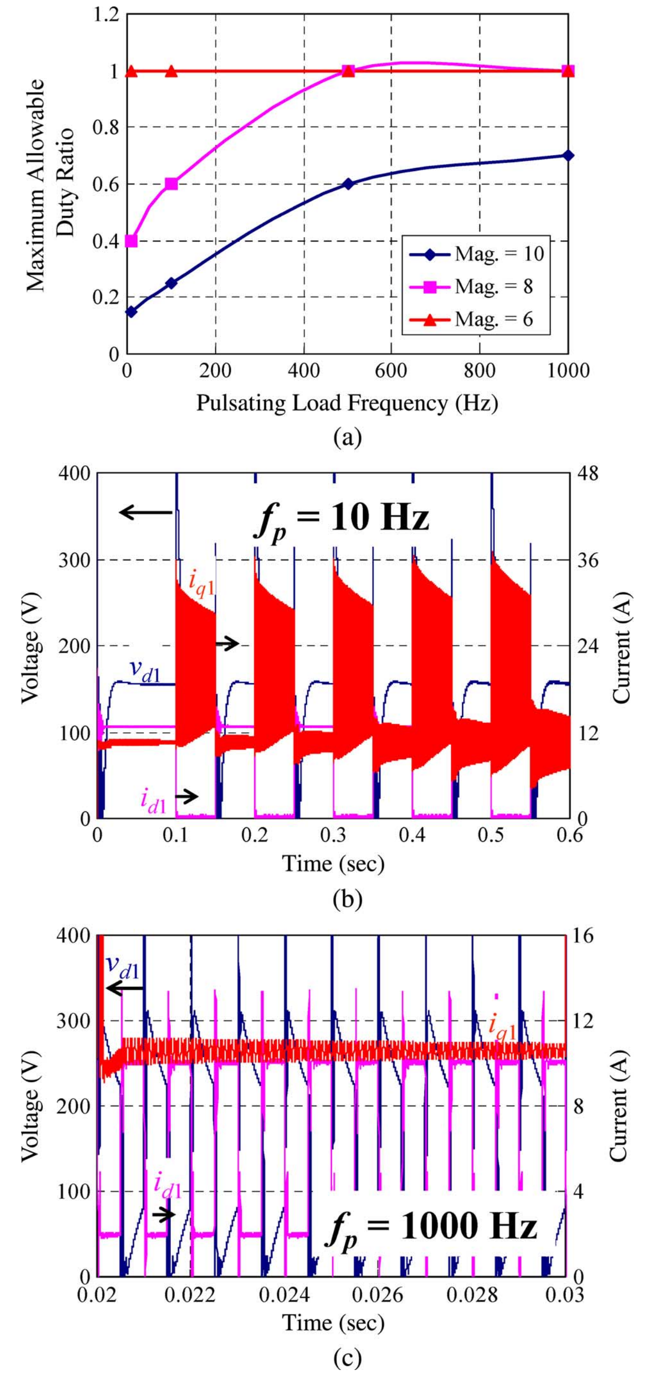

Fig. 11. (a) Variations of the maximum allowable duty ratio with perturbation frequency for pulsating load magnitudes of $\Delta d = 10$ A, $\Delta d = 8$ A, and $\Delta d = 6$ A. (b) and (c) Simulation results illustrating the dynamics of the three-phase VSI with a pulsating load for (b) $f_p = 10$ Hz and (c) $f_p = 1000$ Hz. For the simulation results in (b) and (c), $\Delta d = 10$ A, and $D_p = 50\%$.

Fig. 10 also indicates that the reachable region can vary with the frequency of the load pulse. We plot the variation of the reachable region with the load pulse frequency in Fig. 11.

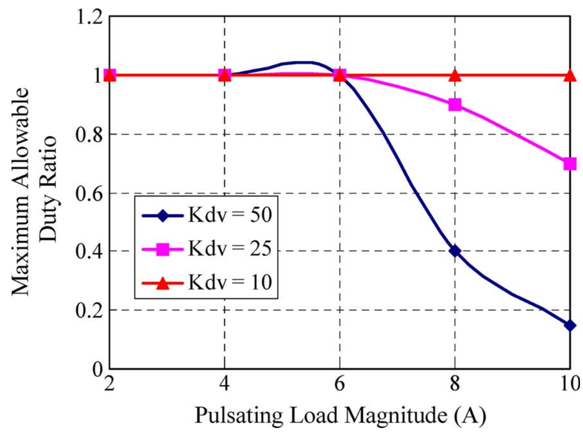

Fig. 12. Variations of the maximum allowable duty ratio with perturbation magnitude for $K_{dv} = 50$, $K_{dv} = 25$, and $K_{dv} = 10$.

From Fig. 11, we observe that, for high magnitudes of the pulsating load amplitude, the region of reachable operation significantly reduces for low pulsating load frequencies. For the case considered in this paper, the region of reachable operation does not change with frequency for pulsating load magnitudes lower than $\Delta d = 6$ A. The simulation results in Fig. 11(b) and (c) validate these predictions.

We note that the results presented so far in this section are for the nominal parameters of the closed-loop controller given in Table II. The region of reachable operation can also be altered by variations of the controller parameters. For instance, Fig. 12 illustrates the variation of the maximum allowable duty ratio of the pulsating load with variations of its magnitude for three different values of the d-axis voltage-loop gain K_{dv}. We observe that the region of reachable operation increases as K_{dv} decreases. Similar analyses can be performed for other controller parameters as well, and appropriate controller parameters can be chosen, depending on the application.

C. Diode Rectifier Load

Next, we investigate how the reaching criterion can be extended to the case of a nonlinear diode rectifier load. The PWL model of the overall system (comprising the three-phase VSI and the diode rectifier) is described in Section II. For the diode rectifier load, there are additional switching states due to the voltage-dependent switching of the diodes. Fig. 13 illustrates two simulation results that are obtained by implementing the PWL models of the overall system. Clearly, for one case, the d-axis voltage-error trajectories converge to the orbit, whereas, for the other case, they do not. As for passive loads, the simulation results agree with the predictions of the reaching criterion derived in Section III. Fig. 14 illustrates the variations of the minimum eigenvalues of the augmented P and Q matrices [obtained by solving LMIs (19) and (22), respectively] with variation of the VSI output voltage (v_{a_1}, v_{b_1}, v_{c_1}) total harmonic distortion (THD) for the diode rectifier load. As in the case of passive loads, distinction among the sliding-mode and asymptotic mode of convergence is obtained using the criteria described in [20]. The THD is varied by changing the values of the load inductors (L_{a2}, L_{b2}, and L_{c2}) and the output capacitor (C_D) of the diode rectifier load. In Fig. 14,

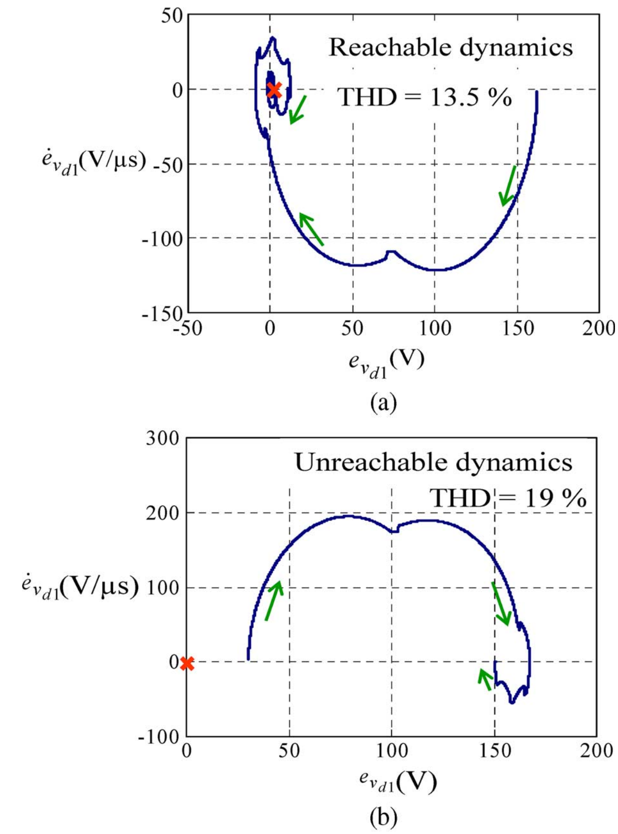

Fig. 13. Simulation results illustrating the d-axis voltage-error trajectories for a three-phase VSI connected to a diode rectifier with a voltage-loop gain of $K_{dv} = 250$ for the following load THDs: (a) 13.5% and (b) 19.8%.

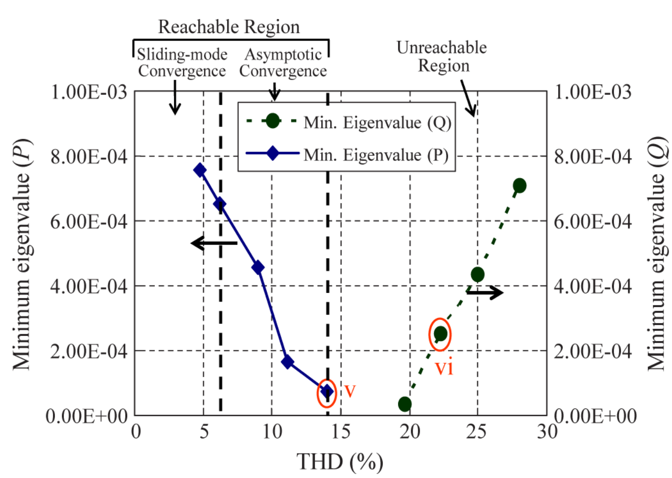

Fig. 14. Plot showing the variation of the minimum eigenvalues of the augmented P and Q matrices [obtained by solving LMIs (19) and (22), respectively] with the output-voltage THD for a three-phase VSI with diode rectifier load. The solid and dashed lines correspond to the *reachable* and *unreachable* regions, respectively.

the range of THD is thus chosen, because it accounts for the reachable and unreachable regions of operation. Time-domain results are only illustrated for one reachable case and one unreachable case. Above a THD of 19%, the dynamics are expected to be unreachable for the VSI-load system considered in this paper. Comparison of these results with those in Fig. 4(a) illustrates that, for a given value of voltage-loop gain K_{dv} (for a load-phase angle $\phi = 30°$ and an apparent power of 2.5 kVA),

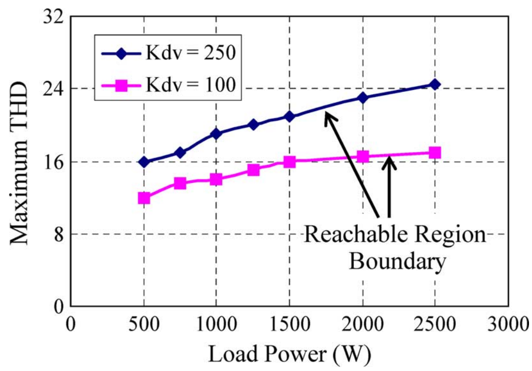

Fig. 15. Variation of the reaching conditions of the VSI-load system with changes in the load power and the d-axis voltage-loop compensator gain for a diode rectifier load.

the reachable region for the passive load is higher than that for the nonlinear loads. Furthermore, variation of the reaching conditions of the VSI with load power and the gain of the d-axis voltage-loop compensator is illustrated in Fig. 15. From Fig. 15, we observe that the region of reachable operation shrinks with decrease in the load power and is also dependent on K_{dv}. Similar analyses of the reaching conditions with other controller parameters can help in designing controllers that ensure the global stability of the VSI-load system for different operating conditions.

Finally, the steady-state stability of the system can be predicted by using the CLF-based approach [given by (23)], as illustrated in Fig. 16(a), and the impedance criterion [given by (24)], as illustrated in Fig. 16(b). The small-signal impedance of the diode rectifier is obtained using the impedance matching procedure described in [36]. In Fig. 16(b), we illustrate only the positive-sequence small-signal impedance. The negative-sequence and zero-sequence small-signal impedances also yield similar results. For this case, the region of "steady-state" stable operation and the region of reachable operation are the same.

VI. Summary and Conclusion

We develop a methodology to investigate the impacts of passive (*RL* and *RC*) and nonlinear (diode rectifier) loads on the reaching conditions of a three-phase VSI. Using CLFs, the reaching criterion is developed for PWL models of the VSI and the loads. The predictions of the reaching criterion are validated by time-domain simulation results. Furthermore, the CLF-based approach is extended to investigate the stability of the nominal (period-1) orbit. Such a technique can be used to predict the fast-scale as well as slow-scale dynamics of the system without the computational overhead of solving complex nonlinear maps. Comparisons of the predictions of the reaching criterion with those of the steady-state stability analyses (based on CLF as well as the small-signal impedance criterion) demonstrate the need for the reaching criterion to predict the global stability of the VSI-load system. Using some specific examples, we demonstrate how, under certain operating conditions, although the system satisfies the steady-state stability criteria, its reaching conditions are not guaranteed. The simulation results show that the state-error trajectories will approach the equilibrium orbit, provided that the initial condition lies within its vicinity; however, its reachability from any arbitrary initial condition is not guaranteed. This discrepancy is because the steady-state stability analysis techniques assume the existence of an orbit. However, for global stability of the system, it is necessary to first ascertain orbital existence (which can be predicted by the reaching criterion described in this paper).

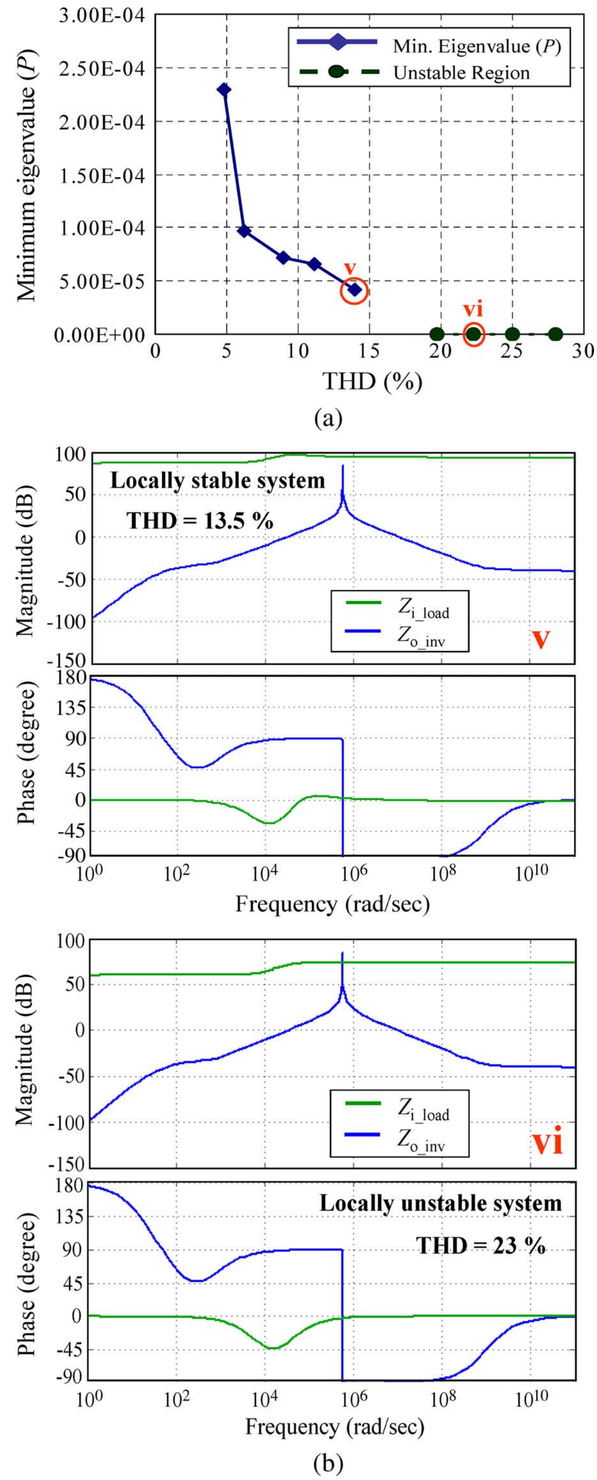

Fig. 16. (a) Variation of the minimum eigenvalue of the augmented P matrix [obtained by solving (19)] of a three-phase VSI (with a voltage-loop gain of $K_{dv} = 250$) with the THD for operating conditions where the system exhibits period-1 stability. (b) Variation of the small-signal output impedance of the VSI and the input impedance of the diode rectifier load for the cases marked (v) and (vi) in Figs. 14 and 16(a).

Furthermore, the predictions of the reaching criterion for the VSI-load system indicate that the range of reachable operating conditions can significantly vary for different types of loads. For instance, for the same apparent power and load phase angles, higher values of voltage-loop gains are required to ensure the reachability for the case of the diode rectifier load, as compared to the passive loads. We observe that variations of the nature of the load and the power drawn by it can also have an impact on the reaching conditions of the overall system. Furthermore, we demonstrate that, for periodically pulsating loads, the reaching conditions can vary (compared to reaching condition predictions with constant loads) with changes in the duty ratio of the load pulse. The analysis in this paper demonstrates that the reaching conditions of the system vary with changes in the voltage-loop compensator gains. Similar results can be obtained for the variation of other controller parameters as well. Thus, the predictions of the reaching criterion can be used to select controller gains and bandwidths that increase the region of globally stable operation of the VSI for different load/operating conditions.

However, the analysis procedure presented in this paper has to be further modified to account for smooth nonlinear loads (for instance, an inverter supplying a motor load), where the system equations are described by piecewise nonlinear models. The analysis procedure can also be extended to other power converter types as well as interconnected networks of converters, such as parallel or cascaded connection, with appropriate modifications to account for the interconnection effects. These issues are part of our current research focus.

APPENDIX
DEFINITIONS OF MATRICES FOR THE PWL MODELS OF THE THREE-PHASE VSI WITH DIFFERENT LOAD TYPES

A. Inductive Load

For the inductive load, the definitions of the various vectors and matrices that are described in Section II are given as follows:

$$i_1^{abc} = \begin{bmatrix} i_{a\_1} \\ i_{b\_1} \\ i_{c\_1} \end{bmatrix} \quad v_1^{abc} = \begin{bmatrix} v_{a\_1} \\ i_{b\_1} \\ i_{c\_1} \end{bmatrix}$$

$$i_2^{abc} = \begin{bmatrix} i_{a\_2} \\ i_{b\_2} \\ i_{c\_2} \end{bmatrix} \quad v_2^{abc} = \begin{bmatrix} v_{a\_2} \\ i_{b\_2} \\ i_{c\_2} \end{bmatrix}$$

$$K_1 = \begin{bmatrix} -\frac{(r_{L1}+r_{C1})}{L_1} & 0 & 0 \\ 0 & -\frac{(r_{L1}+r_{C1})}{L_1} & 0 \\ 0 & 0 & -\frac{(r_{L1}+r_{C1})}{L_1} \end{bmatrix}$$

$$K_2 = \begin{bmatrix} -\frac{r_{C1}}{L_1} & 0 & 0 \\ 0 & -\frac{r_{C1}}{L_1} & 0 \\ 0 & 0 & -\frac{r_{C1}}{L_1} \end{bmatrix}$$

$$K_3 = \begin{bmatrix} -\frac{1}{L_1} & 0 & 0 \\ 0 & -\frac{1}{L_1} & 0 \\ 0 & 0 & -\frac{1}{L_1} \end{bmatrix} \quad K_4 = 0_{3\times 3}$$

$$K_5 = \begin{bmatrix} \frac{2}{3L_1}(2S_{a1} - S_{b1} - S_{c1}) \\ \frac{2}{3L_1}(2S_{b1} - S_{c1} - S_{a1}) \\ \frac{2}{3L_1}(2S_{c1} - S_{a1} - S_{b1}) \end{bmatrix}$$

$$K_6 = \begin{bmatrix} \frac{1}{C_1} & 0 & 0 \\ 0 & \frac{1}{C_1} & 0 \\ 0 & 0 & \frac{1}{C_1} \end{bmatrix}$$

$$K_7 = \begin{bmatrix} -\frac{1}{C_1} & 0 & 0 \\ 0 & -\frac{1}{C_1} & 0 \\ 0 & 0 & -\frac{1}{C_1} \end{bmatrix} \quad K_8 = 0_{3\times 3} \quad K_9 = 0_{3\times 3}$$

$K_{10} = 0_{3\times 1}$.

$$\overline{L}_1 = \begin{bmatrix} \frac{r_{C1}}{L_{RL}} & 0 & 0 \\ 0 & \frac{r_{C1}}{L_{RL}} & 0 \\ 0 & 0 & \frac{r_{C1}}{L_{RL}} \end{bmatrix}$$

$$\overline{L}_2 = \begin{bmatrix} -\frac{(R_{RL}+r_{C1})}{L_1} & 0 & 0 \\ 0 & -\frac{(R_{RL}+r_{C1})}{L_1} & 0 \\ 0 & 0 & -\frac{(R_{RL}+r_{C1})}{L_1} \end{bmatrix}$$

$$\overline{L}_3 = \begin{bmatrix} \frac{1}{L_{RL}} & 0 & 0 \\ 0 & \frac{1}{L_{RL}} & 0 \\ 0 & 0 & \frac{1}{L_{RL}} \end{bmatrix}$$

and $\overline{L}_5$–$\overline{L}_{11}$ are $0_{3\times 3}$.

The overall state-space equations of the system in the synchronous reference frame for the inductive load are described by (12). The definitions of the vectors and matrices in (12) are shown at the bottom of the next page. The sensor gain matrix is given by

$$H_p = \begin{bmatrix} 0 & 0 & 0 & 0 & -H_{dv} & 0 \\ 0 & 0 & 0 & 0 & 0 & 0 \\ -H_{di} & 0 & 0 & 0 & 0 & 0 \\ 0 & 0 & 0 & 0 & 0 & 0 \\ 0 & -H_{qi} & 0 & 0 & 0 & 0 \\ 0 & 0 & 0 & 0 & 0 & 0 \end{bmatrix}.$$

B. Capacitive Load

For the capacitive load, the definitions of the various vectors and matrices that are described in Section II are given as follows:

$$i_1^{abc} = \begin{bmatrix} i_{a\_1} \\ i_{b\_1} \\ i_{c\_1} \end{bmatrix} \quad v_1^{abc} = \begin{bmatrix} v_{a\_1} \\ i_{b\_1} \\ i_{c\_1} \end{bmatrix}$$

$$i_2^{abc} = \begin{bmatrix} i_{a\_2} \\ i_{b\_2} \\ i_{c\_2} \end{bmatrix} \quad v_2^{abc} = \begin{bmatrix} v_{a\_2} \\ i_{b\_2} \\ i_{c\_2} \end{bmatrix}$$

$$K_1 = \begin{bmatrix} -\frac{(r_{L1}+r_{C1})}{L_1} & 0 & 0 \\ 0 & -\frac{(r_{L1}+r_{C1})}{L_1} & 0 \\ 0 & 0 & -\frac{(r_{L1}+r_{C1})}{L_1} \end{bmatrix}$$

$$K_2 = \begin{bmatrix} -\frac{r_{C1}}{L_1} & 0 & 0 \\ 0 & -\frac{r_{C1}}{L_1} & 0 \\ 0 & 0 & -\frac{r_{C1}}{L_1} \end{bmatrix}$$

$$K_3 = \begin{bmatrix} -\frac{1}{L_1} & 0 & 0 \\ 0 & -\frac{1}{L_1} & 0 \\ 0 & 0 & -\frac{1}{L_1} \end{bmatrix} \quad K_4 = 0_{3\times 3}$$

$$K_5 = \begin{bmatrix} \frac{2}{3L_1}\left(2S_{a1} - S_{b1} - S_{c1}\right) \\ \frac{2}{3L_1}\left(2S_{b1} - S_{c1} - S_{a1}\right) \\ \frac{2}{3L_1}\left(2S_{c1} - S_{a1} - S_{b1}\right) \end{bmatrix}$$

$$K_6 = \begin{bmatrix} \frac{1}{C_1} & 0 & 0 \\ 0 & \frac{1}{C_1} & 0 \\ 0 & 0 & \frac{1}{C_1} \end{bmatrix}$$

$$K_7 = \begin{bmatrix} -\frac{1}{C_1} & 0 & 0 \\ 0 & -\frac{1}{C_1} & 0 \\ 0 & 0 & -\frac{1}{C_1} \end{bmatrix} \quad K_8 = 0_{3\times 3} \quad K_9 = 0_{3\times 3}$$

$$K_{10} = 0_{3\times 1}.$$

$$\overline{L}_4 = \begin{bmatrix} \frac{1}{C_{RC}} & 0 & 0 \\ 0 & \frac{1}{C_{RC}} & 0 \\ 0 & 0 & \frac{1}{C_{RC}} \end{bmatrix}$$

and $\overline{L}_1$–$\overline{L}_3$ and $\overline{L}_5$–$\overline{L}_{11}$ are $0_{3\times 3}$.

The overall state-space equations of the system in the synchronous reference frame for the capacitive load are described by (12). The definitions of the vectors and matrices in (12) are shown at the bottom of the page. The sensor gain matrix is given by

$$H_p = \begin{bmatrix} 0 & 0 & 0 & 0 & -H_{dv} & 0 \\ 0 & 0 & 0 & 0 & 0 & 0 \\ -H_{di} & 0 & 0 & 0 & 0 & 0 \\ 0 & 0 & 0 & 0 & 0 & 0 \\ 0 & -H_{qi} & 0 & 0 & 0 & 0 \\ 0 & 0 & 0 & 0 & 0 & 0 \end{bmatrix}.$$

C. Diode Rectifier Load

For the diode rectifier load, the definitions of the various vectors and matrices that are described in Section II are given as follows:

$$i_1^{abc} = \begin{bmatrix} i_{a\_1} \\ i_{b\_1} \\ i_{c\_1} \end{bmatrix} \quad v_1^{abc} = \begin{bmatrix} v_{a\_1} \\ i_{b\_1} \\ i_{c\_1} \end{bmatrix}$$

$$i_2^{abc} = \begin{bmatrix} i_{a\_2} \\ i_{b\_2} \\ i_{c\_2} \end{bmatrix} \quad v_2^{abc} = \begin{bmatrix} v_{a\_2} \\ i_{b\_2} \\ i_{c\_2} \end{bmatrix}$$

Inductive Load:

$$x_{dq}(t) = [\, i_{d1} \quad i_{q1} \quad i_{d2} \quad i_{q2} \quad v_{d1} \quad v_{q1} \,]^T$$

$$B_{dq\_i} = \left[\frac{4}{3L_1}\left(S_{d1} - \frac{1}{2}S_{q1}\right)V_{\text{in}} \; \frac{4}{3L_1}\left(S_{q1} - \frac{1}{2}S_{d1}\right)V_{\text{in}} \quad 0 \quad 0 \quad 0 \quad 0 \quad \right]^T$$

$$A_{dq\_i} = \begin{bmatrix} -\frac{1}{L_1}(r_{L1} + r_{C1}) & -\omega & \frac{r_{C1}}{L_1} & 0 & -\frac{1}{L_1} & 0 \\ -\omega & -\frac{1}{L_1}(r_{L1} + r_{C1}) & 0 & \frac{r_{C1}}{L_1} & 0 & -\frac{1}{L_1} \\ \frac{r_{C1}}{L_{RL}} & 0 & -\frac{1}{L_{RL}}(R_{RL} + r_{C1}) & -\omega & \frac{1}{L_{RL}} & 0 \\ 0 & \frac{r_{C1}}{L_{RL}} & -\omega & -\frac{1}{L_{RL}}(R_{RL} + r_{C1}) & 0 & \frac{1}{L_{RL}} \\ \frac{1}{C_1} & 0 & \frac{1}{C_1} & 0 & 0 & -\omega \\ 0 & \frac{1}{C_1} & 0 & \frac{1}{C_1} & -\omega & 0 \end{bmatrix}$$

Capacitive Load:

$$x_{dq}(t) = [\, i_{d1} \quad i_{q1} \quad v_{d1} \quad v_{q1} \quad v_{d2} \quad v_{q2} \,]^T$$

$$B_{dq\_i} = [\, \tfrac{4}{3L_1}\left(S_{d1} - \tfrac{1}{2}S_{q1}\right)V_{\text{in}} \quad \tfrac{4}{3L_1}\left(S_{q1} - \tfrac{1}{2}S_{d1}\right)V_{\text{in}} \quad 0 \quad 0 \quad 0 \quad 0]^T$$

$$A_{dq\_i} = \begin{bmatrix} -\frac{1}{L_1}\left(r_{L1} + \frac{R_{RC}r_{c1}}{R_{RC}+r_{c1}}\right) & -\omega & -\frac{R_{RC}}{L_1(R_{RC}+r_{c1})} & 0 & -\frac{1}{L_1}\left(\frac{r_{c1}}{R_{RC}+r_{c1}}\right) & 0 \\ -\omega & -\frac{1}{L_1}\left(r_{L1} + \frac{R_{RC}r_{c1}}{R+r_{c1}}\right) & 0 & -\frac{R_{RC}}{L_1(R_{RC}+r_{c1})} & 0 & -\frac{1}{L_1}\left(\frac{r_{c1}}{R_{RC}+r_{c1}}\right) \\ \frac{1}{C_1}\left(\frac{R_{RC}}{R_{RC}+r_{c1}}\right) & 0 & -\frac{1}{C_1(R_{RC}+r_c)} & -\omega & \frac{1}{C_1(R_{RC}+r_c)} & 0 \\ 0 & \frac{1}{C_1}\left(\frac{R_{RC}}{R_{RC}+r_{c1}}\right) & -\omega & -\frac{1}{C_1(R_{RC}+r_c)} & 0 & \frac{1}{C_1(R_{RC}+r_c)} \\ \frac{1}{C_{RC}}\left(\frac{R_{RC}}{R_{RC}+r_{c1}}\right) & 0 & \frac{1}{C_{RC}(R_{RC}+r_c)} & 0 & -\frac{1}{C_{RC}(R_{RC}+r_c)} & -\omega \\ 0 & \frac{1}{C_{RC}}\left(\frac{R_{RC}}{R_{RC}+r_{c1}}\right) & 0 & \frac{1}{C_{RC}(R_{RC}+r_c)} & -\omega & -\frac{1}{C_{RC}(R_{RC}+r_c)} \end{bmatrix}$$

$$K_1 = \begin{bmatrix} -\frac{(r_{L1}+r_{C1})}{L_1} & 0 & 0 \\ 0 & -\frac{(r_{L1}+r_{C1})}{L_1} & 0 \\ 0 & 0 & -\frac{(r_{L1}+r_{C1})}{L_1} \end{bmatrix}$$
$$K_2 = \begin{bmatrix} -\frac{r_{C1}}{L_1} & 0 & 0 \\ 0 & -\frac{r_{C1}}{L_1} & 0 \\ 0 & 0 & -\frac{r_{C1}}{L_1} \end{bmatrix}$$
$$K_3 = \begin{bmatrix} -\frac{1}{L_1} & 0 & 0 \\ 0 & -\frac{1}{L_1} & 0 \\ 0 & 0 & -\frac{1}{L_1} \end{bmatrix} \quad K_4 = 0_{3\times 3}$$
$$K_5 = \begin{bmatrix} \frac{2}{3L_1}(2S_{a1} - S_{b1} - S_{c1}) \\ \frac{2}{3L_1}(2S_{b1} - S_{c1} - S_{a1}) \\ \frac{2}{3L_1}(2S_{c1} - S_{a1} - S_{b1}) \end{bmatrix}$$
$$K_6 = \begin{bmatrix} \frac{1}{C_1} & 0 & 0 \\ 0 & \frac{1}{C_1} & 0 \\ 0 & 0 & \frac{1}{C_1} \end{bmatrix}$$
$$K_7 = \begin{bmatrix} -\frac{1}{C_1} & 0 & 0 \\ 0 & -\frac{1}{C_1} & 0 \\ 0 & 0 & -\frac{1}{C_1} \end{bmatrix} \quad K_8 = 0_{3\times 3} \quad K_9 = 0_{3\times 3}$$
$$K_{10} = 0_{3\times 1}.$$
$$\overline{L}_7 = \begin{bmatrix} \frac{r_{C1}}{L_2} & 0 & 0 \\ 0 & \frac{r_{C1}}{L_2} & 0 \\ 0 & 0 & \frac{r_{C1}}{L_2} \end{bmatrix}$$
$$\overline{L}_8 = \begin{bmatrix} \frac{r_{L_2}}{L_2} & 0 & 0 \\ 0 & \frac{r_{L_2}}{L_2} & 0 \\ 0 & 0 & \frac{r_{L_2}}{L_2} \end{bmatrix}$$
$$\overline{L}_9 = \begin{bmatrix} \frac{2}{3L_2}(2S_{a2} - S_{b2} - S_{c2}) \\ \frac{2}{3L_2}(2S_{b2} - S_{c2} - S_{a2}) \\ \frac{2}{3L_2}(2S_{c2} - S_{a2} - S_{b2}) \end{bmatrix}$$
$$\overline{L}_{10} = \begin{bmatrix} \frac{S_{a2}}{C_D} & \frac{S_{b2}}{C_D} & \frac{S_{c2}}{C_D} \end{bmatrix}$$

$\overline{L}_{11} = -1/R_D C_D$, and $\overline{L}_1$–$\overline{L}_6$ are $0_{3\times 3}$.

The switching functions of the diode rectifier load can be described as follows:

$$S_{a2} = \begin{cases} 1, & v_{a3} - v_D > 0 \\ -1, & v_{a3} - v_D < 0 \\ 0, & v_{a3} - v_D = 0 \end{cases}$$
$$S_{b2} = \begin{cases} 1, & v_{b3} - v_D > 0 \\ -1, & v_{b3} - v_D < 0 \\ 0, & v_{b3} - v_D = 0 \end{cases}$$
$$S_{c2} = \begin{cases} 1, & v_{c3} - v_D > 0 \\ -1, & v_{c3} - v_D < 0 \\ 0, & v_{c3} - v_D = 0 \end{cases}$$

where

$$v_{a3} = v_{a2} - L_2 \frac{di_{a\_2}}{dt} - i_{a\_2} r_{L_2}$$
$$v_{b3} = v_{b2} - L_2 \frac{di_{b\_2}}{dt} - i_{b\_2} r_{L_2}$$
$$v_{c3} = v_{c2} - L_2 \frac{di_{c\_2}}{dt} - i_{c\_2} r_{L_2}.$$

To test the efficacy of the PWL model, we compare the states of this model with that predicted by Saber, which is a standard simulation package for power electronics simulations. We note that, in the Saber model, we use ideal diodes (i.e., that they have zero ON-state drop, negligible rise and fall times, and no reverse recovery). Fig. 17 illustrates that there is a one-to-one match between the two models. We note here that, for both the models, we choose a fixed sampling step (i.e., 10 μs).

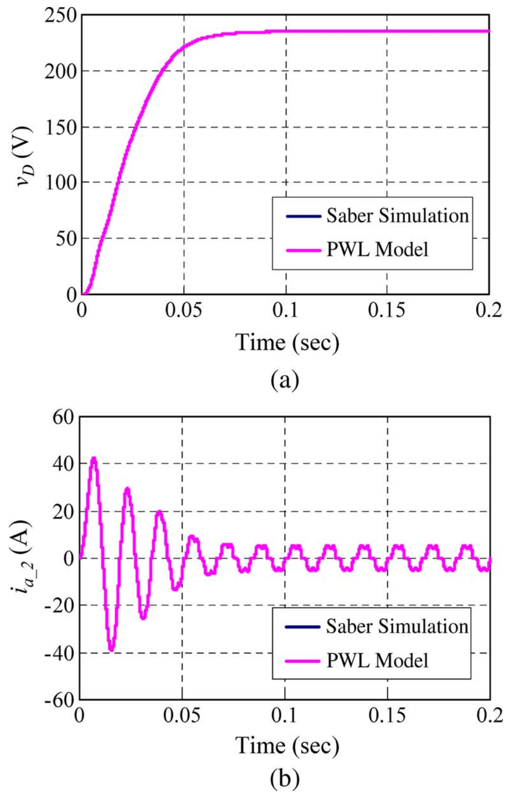

Fig. 17. Comparison of the output voltage and input current of the diode rectifier predicted by the PWL model with those predicted by a Saber [37] simulation of the diode rectifier load.

The overall state-space equations of the system in the synchronous reference frame for the diode rectifier load are described by (12). The definitions of the vectors and matrices in (12) are given as follows:

$$x_{dq}(t) = \begin{bmatrix} i_{d1} & i_{q1} & i_{d2} & i_{q2} & v_{d1} & v_{q1} & v_D \end{bmatrix}^T$$
$$B_{dq\_i} = \begin{bmatrix} \frac{S_{d1}}{L_1} V_{\text{in}} & \frac{S_{q1}}{L_1} V_{\text{in}} & 0 & 0 & 0 & 0 & 0 \end{bmatrix}^T$$
$$A_{dq\_i} = \begin{bmatrix} a_{11} & a_{12} & a_{13} & a_{14} & a_{15} & a_{16} & a_{17} \\ a_{21} & a_{22} & a_{23} & a_{24} & a_{25} & a_{26} & a_{27} \\ a_{31} & a_{32} & a_{33} & a_{34} & a_{35} & a_{36} & a_{37} \\ a_{41} & a_{42} & a_{43} & a_{44} & a_{45} & a_{46} & a_{47} \\ a_{51} & a_{52} & a_{53} & a_{54} & a_{55} & a_{56} & a_{57} \\ a_{61} & a_{62} & a_{63} & a_{64} & a_{65} & a_{66} & a_{67} \\ a_{71} & a_{72} & a_{73} & a_{74} & a_{75} & a_{76} & a_{77} \end{bmatrix}$$

where the elements of A_{dq_i} are given as follows:

$$a_{11} = -\frac{1}{L_1}\left(r_{L1} + \frac{r_{C1}}{1 + \omega^2 r_{C1}^2 C_1^2} \right)$$
$$a_{12} = \omega \left(1 - \frac{C_1 r_{C1}^2}{L_1 (1 + \omega^2 r_{C1}^2 C_1^2)} \right)$$

$$a_{13} = \frac{1}{L_1}\frac{r_{C1}}{1+\omega^2 r_{C1}^2 C_1^2} \quad a_{14} = \frac{1}{L_1}\frac{\omega r_{C1}^2 C_1}{(1+\omega^2 r_{C1}^2 C_1^2)}$$

$$a_{15} = -\frac{1}{L_1}\frac{1}{1+\omega^2 r_{C1}^2 C_1^2} \quad a_{16} = -\frac{\omega r_{C1} C_1}{L_1 (1+\omega^2 r_{C1}^2 C_1^2)}$$

$$a_{17} = 0 \quad a_{21} = -\omega\left(1 - \frac{C_1 r_{C1}^2}{L_1 (1+\omega^2 r_{C1}^2 C_1^2)}\right)$$

$$a_{22} = -\frac{1}{L_1}\left(r_{L1} + \frac{r_{C1}}{1+\omega^2 r_{C1}^2 C_1^2}\right)$$

$$a_{23} = \frac{1}{L_1}\frac{\omega r_{C1}^2 C_1}{(1+\omega^2 r_{C1}^2 C_1^2)} \quad a_{24} = \frac{1}{L_1}\frac{r_{C1}}{(1+\omega^2 r_{C1}^2 C_1^2)}$$

$$a_{25} = \frac{\omega r_{C1} C_1}{L_1 (1+\omega^2 r_{C1}^2 C_1^2)} \quad a_{26} = 0 \quad a_{27} = 0$$

$$a_{31} = \frac{1}{L_2}\frac{r_{C1}}{(1+\omega^2 r_{C1}^2 C_1^2)} \quad a_{32} = \frac{1}{L_2}\frac{\omega r_{C1}^2 C_1}{(1+\omega^2 r_{C1}^2 C_1^2)}$$

$$a_{33} = -\frac{1}{L_2}\left(\frac{r_{C1}}{1+\omega^2 r_{C1}^2 C_1^2} + r_{L2} + \frac{3}{2}\frac{R_L r_{C2}}{R_L + r_{C2}} S_{d2}^2\right)$$

$$a_{34} = \frac{1}{L_2}\left(\omega L_2 - \frac{3}{2}\frac{R_L r_{C2}}{R_L + r_{C2}} S_{d2} S_{q2} - \frac{\omega r_{C1}^2 C_1}{(1+\omega^2 r_{C1}^2 C_1^2)}\right)$$

$$a_{35} = \frac{1}{L_2}\frac{1}{(1+\omega^2 r_{C1}^2 C_1^2)} \quad a_{36} = \frac{1}{L_2}\frac{\omega r_{C1} C_1}{(1+\omega^2 r_{C1}^2 C_1^2)}$$

$$a_{37} = -\frac{1}{L_2}\frac{R_L}{R_L + r_{C2}} S_{d2} \quad a_{41} = -\frac{1}{L_2}\frac{\omega r_{C1}^2 C_1}{(1+\omega^2 r_{C1}^2 C_1^2)}$$

$$a_{42} = \frac{1}{L_2}\frac{r_{C1}}{(1+\omega^2 r_{C1}^2 C_1^2)}$$

$$a_{43} = -\frac{1}{L_2}\left(\omega L_2 + \frac{3}{2}\frac{R_D r_{C2}}{R_D + r_{C2}} S_{d2} S_{q2} - \frac{\omega r_{C1}^2 C_1}{(1+\omega^2 r_{C1}^2 C_1^2)}\right)$$

$$a_{44} = -\frac{1}{L_2}\left(\frac{r_{C1}}{(1+\omega^2 r_{C1}^2 C_1^2)} + r_{L2}\right)$$

$$a_{45} = -\frac{1}{L_2}\frac{\omega r_{C1} C_1}{(1+\omega^2 r_{C1}^2 C_1^2)} \quad a_{46} = \frac{1}{L_2}\frac{1}{(1+\omega^2 r_{C1}^2 C_1^2)}$$

$$a_{47} = \frac{R_D}{L_2} S_{q2} \quad a_{51} = \frac{1}{C_1}\left(\frac{1}{(1+\omega^2 r_{C1}^2 C_1^2)}\right)$$

$$a_{52} = \frac{\omega r_{C1}}{(1+\omega^2 r_{C1}^2 C_1^2)} \quad a_{53} = -\frac{1}{C_1 (1+\omega^2 r_{C1}^2 C_1^2)}$$

$$a_{54} = -\frac{\omega r_{C1}}{(1+\omega^2 r_{C1}^2 C_1^2)} \quad a_{55} = -\frac{\omega^2 r_{C1} C_1}{(1+\omega^2 r_{C1}^2 C_1^2)}$$

$$a_{56} = \frac{\omega}{(1+\omega^2 r_{C1}^2 C_1^2)} \quad a_{57} = 0 \quad a_{61} = -\frac{\omega r_{C1}}{(1+\omega^2 r_{C1}^2 C_1^2)}$$

$$a_{62} = \frac{1}{C_1}\left(\frac{1}{(1+\omega^2 r_{C1}^2 C_1^2)}\right) \quad a_{63} = -\frac{\omega r_{C1}}{(1+\omega^2 r_{C1}^2 C_1^2)}$$

$$a_{64} = -\frac{1}{C_1 (1+\omega^2 r_{C1}^2 C_1^2)} \quad a_{65} = -\frac{\omega}{(1+\omega^2 r_{C1}^2 C_1^2)}$$

$$a_{66} = -\frac{\omega^2 r_{C1} C_1}{(1+\omega^2 r_{C1}^2 C_1^2)} \quad a_{67} = 0$$

$$a_{71} = 0 \quad a_{72} = 0 \quad a_{73} = \frac{3}{2}\frac{R_D}{R_D C_D + r_{C1} C_D} S_{d2}$$

$$a_{74} = \frac{3}{2}\frac{R_D}{R_D C_D + r_{C1} C_D} S_{q2} \quad a_{75} = 0 \quad a_{76} = 0$$

$$a_{77} = -\frac{1}{R_D C_D + r_{C1} C_D}.$$

The sensor gain matrix is given by

$$H_p = \begin{bmatrix} 0 & 0 & 0 & 0 & -H_{dv} & 0 & 0 \\ 0 & 0 & 0 & 0 & 0 & 0 & 0 \\ -H_{di} & 0 & 0 & 0 & 0 & 0 & 0 \\ 0 & 0 & 0 & 0 & 0 & 0 & 0 \\ 0 & -H_{qi} & 0 & 0 & 0 & 0 & 0 \\ 0 & 0 & 0 & 0 & 0 & 0 & 0 \end{bmatrix}.$$

ACKNOWLEDGMENT

Any opinions, findings, conclusions, or recommendations expressed herein are those of the authors and do not necessarily reflect the views of NSF and ONR.

REFERENCES

[1] R. D. Middlebrook, "Input filter considerations in design and application of switching regulators," in *Advances in Switch-Mode Power Conversion*, 2nd ed. Pasadena, CA: TESLAco, 1983, pp. 91–107.

[2] S. S. Kelkar and F. C. Lee, "A novel input filter compensation scheme for switching regulators," in *Proc. IEEE Power Electron. Spec. Conf.*, Jun. 1982, pp. 260–271.

[3] Y. E. Sandra and W. A. Polivka, "Input filter design criteria for current-programmed regulators," *IEEE Trans. Power Electron.*, vol. 7, no. 1, pp. 143–151, Jan. 1992.

[4] L. R. Lewis, B. H. Cho, F. C. Lee, and B. A. Carpenter, "Modeling, analysis and design of distributed power systems," in *Proc. IEEE Power Electron. Spec. Conf.*, Jun. 1989, vol. 1, pp. 152–159.

[5] C. M. Wildrick, F. C. Lee, B. H. Cho, and B. Choi, "A method of defining the load impedance specification for a stable distributed power system," *IEEE Trans. Power Electron.*, vol. 10, no. 3, pp. 280–285, May 1995.

[6] X. Wang, R. Yao, and F. Rao, "Three-step impedance criterion for small-signal stability analysis in two-stage DC distributed power systems," *IEEE Power Electron. Lett.*, vol. 1, no. 3, pp. 83–87, Sep. 2003.

[7] S. Chandrasekaran, D. Borojevic, and D. K. Lindner, "Input filter interaction in three-phase AC-DC converters," in *Proc. IEEE Power Electron. Spec. Conf.*, Jun. 1999, vol. 2, pp. 987–992.

[8] S. K. Mazumder, A. H. Nayfeh, and D. Boroyevich, "Theoretical and experimental investigation of the fast- and slow-scale instabilities of a DC-DC converter," *IEEE Trans. Power Electron.*, vol. 16, no. 2, pp. 201–216, Mar. 2001.

[9] R. Zhang, "High performance power converter systems for nonlinear and unbalanced load/source," Ph.D. dissertation, Dept. Elect. and Comput. Eng. Virginia Polytechnic Inst. and State Univ., Blacksburg, VA, Nov. 1998.

[10] H. R. Visser and P. P. J. van den Bosch, "Modelling of periodically switching networks," in *Proc. IEEE Power Electron. Spec. Conf.*, Jun. 1991, pp. 67–73.

[11] R. Leyva, I. Queinnec, S. Tarbouriech, C. Alonso, and L. Martinez-Salamero, "Large-signal stability in high-order switching converters," in *Proc. IEEE Amer. Control Conf.*, Jun. 2004, pp. 59–64.

[12] D. Casadei, J. Clare, L. Empringham, G. Serra, A. Tani, A. Trentin, P. Wheeler, and L. Zarri, "Large-signal model for the stability analysis of matrix converters," *IEEE Trans. Ind. Electron.*, vol. 54, no. 2, pp. 939–950, Apr. 2007.

[13] C. C. Chan and K.-T. Chau, "A fast and exact time-domain simulation of switched-mode power regulators," *IEEE Trans. Ind. Electron.*, vol. 39, no. 4, pp. 341–350, Aug. 1992.

[14] S. Ben-Yaakov, S. Glozman, and R. Rabinovici, "Envelope simulation by SPICE-compatible models of electric circuits driven by modulated signals," *IEEE Trans. Ind. Electron.*, vol. 47, no. 1, pp. 222–225, Feb. 2000.

[15] R. W. Erickson, S. Cuk, and R. D. Middlebrook, "Large-signal modelling and analysis of switching regulators," in *Proc. IEEE Power Electron. Spec. Conf.*, Jun. 1982, pp. 240–250.

[16] V. Utkin, *Sliding Modes in Control Optimization*. New York: Springer-Verlag, 1992.

[17] A. F. Filippov, *Differential Equations With Discontinuous Right Hand Sides*. Dordrecht, The Netherlands: Kluwer, 1988.

[18] D. Milosavljevic, "General conditions for the existence of a quasi-sliding mode on the switching hyperplane in discrete variable structure systems," *Autom. Remote Control*, vol. 46, no. 3, pp. 307–314, 1985.

[19] S. K. Mazumder and K. Acharya, "Multiple Lyapunov function based reaching condition analyses of switching power converters," in *Proc. IEEE Power Electron. Spec. Conf.*, Jun. 2006, pp. 2232–2239.

[20] S. K. Mazumder and K. Acharya, "Multiple Lyapunov function based reaching condition for orbital existence of switching power converters," *IEEE Trans. Power Electron.*, May 2008, to be published.

[21] G. Escobar, P. Mattavelli, A. M. Stankovic, A. A. Valdez, and J. Leyva-Ramos, "An adaptive control for UPS to compensate unbalance and harmonic distortion using a combined capacitor/load current sensing," *IEEE Trans. Ind. Electron.*, vol. 54, no. 2, pp. 839–847, Apr. 2007.

[22] G. Willmann, D. F. Coutinho, L. F. A. Pereira, and F. B. Libano, "Multiple-loop H-infinity control design for uninterruptible power supplies," *IEEE Trans. Ind. Electron.*, vol. 54, no. 3, pp. 1591–1602, Jun. 2007.

[23] M. Dai, M. N. Marwali, J. W. Jung, and A. Keyhani, "Power flow control of a single distributed generation unit with nonlinear local load," in *Proc. IEEE Power Syst. Conf. Expo.*, Oct. 2004, vol. 1, pp. 398–403.

[24] S. K. Mazumder, "A novel discrete control strategy for independent stabilization of parallel three-phase boost converters by combining space-vector modulation with variable-structure control," *IEEE Trans. Power Electron.*, vol. 18, no. 4, pp. 1070–1083, Jul. 2003.

[25] [Online]. Available: http://mathworld.wolfram.com/FourierSeries.html

[26] R. Marino, G. L. Santosuosso, and P. Tomei, "Robust adaptive compensation of biased sinusoidal disturbances with unknown frequency," *Automatica*, vol. 39, no. 10, pp. 1755–1761, Oct. 2003.

[27] M. Johansson, *Piecewise Linear Control Systems*. New York: Springer-Verlag, 2002.

[28] G. Feng, "Stability analysis of piecewise discrete-time linear systems," *IEEE Trans. Autom. Control*, vol. 47, no. 7, pp. 1108–1112, Jul. 2002.

[29] R. Goebel, T. Hu, and A. R. Teel, "Dual matrix inequalities in stability and performance analysis of linear differential/difference inclusions," in *Current Trends in Nonlinear Systems and Control*. Boston, MA: Birkhauser, 2005.

[30] S. K. Mazumder, A. H. Nayfeh, and D. Boroyevich, "A new approach to the stability analysis of boost power-factor-correction circuits," *J. Vib. Control—Special Issue Nonlinear Dynamics Control*, vol. 9, no. 7, pp. 749–773, 2003.

[31] A. H. Nayfeh and B. Balachandran, *Applied Nonlinear Dynamics*. New York: Wiley, 1995.

[32] *Nonlinear Phenomena in Power Electronics: Attractors, Bifurcations, Chaos, and Nonlinear Control*, S. Banerjee and G. C. Verghese, Eds. New York: IEEE Press, 2001.

[33] C. K. Tse, *Complex Behavior of Switching Power Converters*. New York: CRC Press, 2004.

[34] K. Acharya, S. K. Mazumder, and M. Tahir, "Communication fault-tolerant wireless network control of a load-sharing multiphase interactive power network," in *Proc. IEEE Power Electron. Spec. Conf.*, Jun. 2006, pp. 1167–1174.

[35] V. Lakshmikantham, S. Leela, and A. A. Martynyuk, *Practical Stability of Nonlinear Systems*. Hackensack, NJ: World Scientific, 1990.

[36] Z. Bing, K. Karimi, and J. Sun, "Input impedance modeling and analysis of line-commutated rectifiers," in *Proc. IEEE Power Electron. Spec. Conf.*, Jun. 2007, pp. 1981–1987.

[37] [Online]. Available: http://www.synopsys.com/products/mixedsignal/saber/saber.html

Kaustuva Acharya (S'00) received the B.Eng. degree in electronics and communication engineering from the Regional Engineering College (now the National Institute of Technology), Bhopal, India, in 2000 and the M.Sc. degree in electrical engineering from the University of Illinois, Chicago, in 2003. He is currently working toward the Ph.D. degree in electrical engineering at the University of Illinois.

He is a Research Assistant in the Laboratory for Energy and Switching-Electronics Systems, Department of Electrical and Computer Engineering, University of Illinois. He has published more than 15 refereed international journal and conference papers. His research interests include power electronics for renewable and alternate energy sources, and modeling, analysis, and control of interactive power networks for distributed power systems.

Mr. Acharya is a Reviewer for the IEEE TRANSACTIONS ON POWER ELECTRONICS and the IEEE TRANSACTIONS ON INDUSTRIAL ELECTRONICS, and several international conferences. He copresented a tutorial entitled "Global stability methodologies for switching power converters" at the IEEE Power Electronics Specialists Conference 2007.

Sudip K. Mazumder (SM'02) received the M.S. degree in electrical engineering from Rensselaer Polytechnic Institute (RPI), Troy, NY, in 1993, and the Ph.D. degree in electrical and computer engineering from the Virginia Polytechnic Institute and State University, Blacksburg, in 2001.

He is currently with the Department of Electrical and Computer Engineering, University of Illinois, Chicago, as an Associate Professor and the Director of Laboratory for Energy and Switching-Electronics Systems. He has more than ten years of professional experience and has held R&D and design positions in leading industrial organizations. He has been the Editor-in-Chief for the *International Journal of Power Management Electronics* since 2006. He has published more than 60 refereed and invited journal and conference papers and is a Reviewer for six international journals. His current research interests are interactive power-electronics/power networks, renewable and alternate energy systems, photonically triggered power semiconductor devices, and systems-on-chip/module (i.e., SoC/SoM).

Dr. Mazumder has also been an Associate Editor for the IEEE TRANSACTIONS ON INDUSTRIAL ELECTRONICS since 2003 and was the Associate Editor for the IEEE POWER ELECTRONICS LETTERS until 2005. He has been invited by both the IEEE and the American Society of Mechanical Engineers for several keynote and plenary lectures. He presented a tutorial entitled "Global stability methodologies for switching power converters" at the IEEE Power Electronics Specialists Conference 2007. He was the recipient of the Faculty Research Award (2008) and Diamond Award (2006) from the University of Illinois for his outstanding research performance, the ONR Young Investigator Award (2005), NSF CAREER Award (2003), the DOE SECA Award (2002), and the Prize Paper Award (2002) from the IEEE TRANSACTIONS ON POWER ELECTRONICS and the IEEE Power Electronics Society. He was a corecipient (with his Ph.D. student M. Tahir) of the 2007 IEEE Outstanding Student Paper Award at the IEEE International Conference on Advanced Information Networking and Applications.

Ishita Basu (S'06) received the B.Sc. degree in instrumentation and electronics engineering from Jadavpur University, Kolkata, India, in 2005. She is currently working toward the Ph.D. degree in electrical engineering from the Laboratory for Energy and Switching-Electronics Systems, Department of Electrical and Computer Engineering, University of Illinois, Chicago.